

On the analyticity of the lightest particle mass of Ising field theory in a magnetic field

Hao-Lan Xu^a

^a*C.N. Yang Institute for Theoretical Physics, State University of New York, Stony Brook, NY 11794-3840, USA*

E-mail: hao-lan.xu@stonybrook.edu

ABSTRACT: We study the scaling functions associated with the lightest particle mass M_1 in 2d Ising field theory in external magnetic field. The scaling functions depend on the scaling parameter $\xi = h/|m|^{\frac{15}{8}}$, or related parameter $\eta = m/h^{\frac{8}{15}}$. Analytic properties of M_1 in the high-T domain were discussed in [1]. In this work, we study analyticity of M_1 in the low-T domain. Important feature of this analytic structure is represented by the Fisher-Langer's branch cut. The discontinuity across this branch cut determines the behavior of M_1 at all complex ξ via associated low-T dispersion relation. Also, we put forward the "extended analyticity" conjecture for M_1 in the complex η -plane, similar to the analyticity of the free energy density previously proposed in [2]. The extended analyticity implies the "extended dispersion relation", which we verify against the numerics from the Truncated Free Fermion Approach (TFFSA), giving strong support to the conjecture.

Contents

1	Introduction	1
2	Analyticity of $\hat{M}_p(\xi)$, $p = 1, 2, 3$ and the Fisher-Langer's branch cut	10
3	Extended dispersion relation of M_1	17
4	Summary and discussion	24
A	Numerical approximation of $\Delta_1(y)$ from interpolation	27
B	Computing the non-analytic term \mathcal{K}_p.	28

1 Introduction

The scaling behaviour of Ising model near its ferromagnetic critical point describes one of the most important universality classes of two dimensional criticality, and the related field theory interpretation, known as 2d Ising Field Theory (IFT), is an interesting example of 2d quantum field theory with rich particle spectrum and S-matrices. In this report, as a continuation of previous works [2][3][1][4], we focus on the mass of lightest excitation, denoted as M_1 , and discuss its analytic properties as the function of the scaling parameter.

2d Ising field Theory

At the ferromagnetic critical point $(T, H) = (T_c, 0)$, say at the Curie temperature with no external magnetic field, the scaling limit of Ising model is described by Ising Conformal Field Theory (ICFT), which in two dimension is represented by the minimal CFT $\mathcal{M}_{3,4}$, with Virasoro central charge $c_{3,4} = \frac{1}{2}$. From Wilsonian point of view, the Ising ferromagnetic critical point is a fix point of Renormalization Group (RG) flows. Near the Ising critical point, the scaling limit of 2d Ising model is described by 2d Ising field theory, which alternatively can be understood in terms of the RG flow initiated from the Ising fixed point, generated by perturbing with two relevant operators. The description is given by the formal action:

$$\mathcal{A}_{\text{IFT}} = \mathcal{A}_{\text{FF}} + h \int \sigma(x) d^2x = \mathcal{A}_{3,4}^* + \frac{m}{2\pi} \int \varepsilon(x) d^2x + h \int \sigma(x) d^2x, \quad (1.1)$$

where $\mathcal{A}_{3,4}^*$ is the action of minimal model $\mathcal{M}_{3,4}$, $\sigma(x)$ and $\varepsilon(x)$ are local spin density and energy density operators respectively. The couplings m and h are related to the infinitesimal

deviation from the critical point, say:

$$m \propto \frac{T_c - T}{T_c}, \quad \text{and} \quad h \propto H, \quad (1.2)$$

with the normalization coefficients are fixed by requiring the short-distance behaviours¹:

$$|x|^{\frac{1}{4}} \langle \sigma(x) \sigma(0) \rangle \rightarrow 1, \quad |x|^2 \langle \varepsilon(x) \varepsilon(0) \rangle \rightarrow 1 \quad (1.3)$$

at $x \rightarrow 0$. Note that the two nontrivial local relevant scalar operators $\sigma(x)$ and $\varepsilon(x)$ have the scaling dimensions $(\Delta_\sigma, \bar{\Delta}_\sigma) = (\frac{1}{16}, \frac{1}{16})$ and $(\Delta_\varepsilon, \bar{\Delta}_\varepsilon) = (\frac{1}{2}, \frac{1}{2})$ respectively, hence the corresponding relevant couplings have mass dimensions $[h] = \frac{15}{8}$ and $[m] = 1$. The dimensionless combination

$$\xi = \frac{h}{|m|^{\frac{15}{8}}} \quad \left(\quad \text{or} \quad \eta = \frac{m}{h^{\frac{8}{15}}} \right), \quad (1.4)$$

²labels the renormalization group trajectories stemming from the Ising CFT fixed point. As is conventional, we will call ξ (or η) the scaling parameter.

The scaling behaviour of the IFT is described by dimensionless functions known as scaling functions, which only depend on the scaling parameter ξ or η . In this work, we study the mass of the lightest particle, denoted as $M_1 = M_1(m, h)$. As the energy of lightest excitation, M_1 carries some of the most important information of the theory. In particular, M_1 can be identified with the inverse of correlation length, as $R_c = M_1^{-1}$, and criticality occurs when $M_1 \rightarrow 0$. The scaling functions of M_1 are defined as:

$$\hat{M}_1 = \hat{M}_1(\xi) = M_1/|m|, \quad \text{and} \quad \mathcal{M}_1 = \mathcal{M}_1(\eta) = M_1/|h|^{\frac{8}{15}}. \quad (1.5)$$

Both functions $\hat{M}_1(\xi)$ and $\mathcal{M}_1(\eta)$ can be analytically continued to complex values of the scaling parameters ξ or η . It is the analytic properties of these scaling functions as the functions of complex ξ and η which are studied in this work. Part of the analyticity of $\hat{M}_1(\xi)$ was discussed in [1] in the $m < 0$ high-T regime, while in this work, we will discuss the analyticity of $\hat{M}_1(\xi)$ in the $m > 0$ low-T regime, and the analyticity of $\mathcal{M}_1(\eta)$ on the complex η -plane, which unifies the high-T and low-T analyticities of $\hat{M}_1(\xi)$. We expect the analyticities of $\hat{M}_1(\xi)$ and $\mathcal{M}_1(\eta)$ to be similar to the scaling functions associated with the vacuum energy density $F(m, h)$, which were analyzed in [2].

High-T analyticity of M_1

In this subsection, we briefly review the high-T analyticity of $\hat{M}_1(\xi)$, as discussed in [1]. In the high-T regime $T > T_c$ (equivalently $m < 0$), IFT enjoys the \mathbb{Z}_2 symmetry $h \rightarrow -h$, $\sigma(x) \rightarrow -\sigma(x)$. As the result, all scaling functions should be even functions of ξ . It is conventional to denote instead the scaling function as $\hat{M}_1 = \hat{M}_1(u)$, where $u := \xi^2$. From

¹The proportionality coefficient in (1.2) depends on specific microscopic model, for details, see e.g. [5].

²Depending on the sign of m , η is related to ξ by $\eta = \xi^{-8/15}$ in the low-T regime $m > 0$, or $\eta = -\xi^{-8/15}$ in the high-T regime $m < 0$.

$u > 0$, $\hat{M}_1(u)$ can be analytically continued to generic complex values of u . $\hat{M}_1(u)$ is expected to be analytic everywhere on the complex u -plane, except at the Yang-Lee (YL) branching point and the associated YL branch cut. The Yang-Lee branching point, also known as Yang-Lee edge singularity, is located at $\xi^2 = -\xi_0^2 \approx -0.03583\dots$ [2][1][5]. As in [2][1], we chose the branch cut to extend along the real u -axis, from $u = -\infty$ to $u = -\xi_0^2$. This defines the principle branch of $\hat{M}_1(u)$. The Yang-Lee branch cut represents a line of first order phase transition with complex state functions. The analyticity structure is as shown in Fig.1.

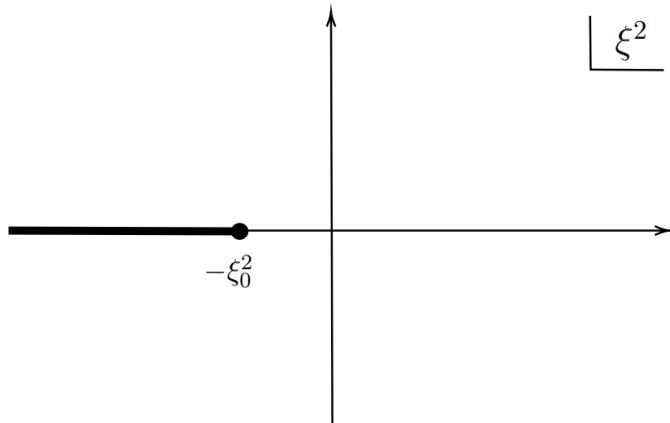


Figure 1. Phase diagram of $\hat{M}_1(u)$ on the complex u -plane, showing high-T standard analyticity. The Yang-Lee singularity is located at $u = -\xi_0^2$, and we choose the Yang-Lee branch cut extends from $u = -\xi_0^2$ to $u = -\infty$. The Yang-Lee branch cut represents a line of first order phase transition with complex state functions.

In fact, in high-T many other scaling functions have similar analyticities on the complex u -plane, as in Fig.1. For example, the scaling functions of free energy density and effective " φ^3 coupling" were discussed in [2] and [4]. This is known as "high-T standard analyticity", which is resulting from the Yang-Lee theorem of Ising ferromagnetic partition function [6][7]. On the lattice, define the fugacity $\mu = e^{-2H/k_B T}$, the Yang-Lee theorem states that zeros of lattice Ising partition function are distributed along the unit circle of the μ -plane, known as the Yang-Lee circle. At $T > T_c$ there is a segment $|\text{Arg } \mu| \leq \text{Arg } \mu_0$ free of any zeros, and the zeros are located on the circle with $|\text{Arg } \mu| > \text{Arg } \mu_0$. In the scaling limit with $T - T_c \rightarrow 0_+$ and $H \rightarrow 0$, the zeros condense into the Yang-Lee branch cut on the complex u -plane, which represents a line of first order phase transition with complex state functions³. The edge of the condensing zeros becomes the Yang-Lee edge singularity, whose location is denoted as $u_0 = -\xi_0^2$. The Yang-Lee edge singularity represents a continuous phase transition, thus is also known as Yang-Lee critical point. The corresponding conformal field theory is the

³With the choice of Yang-Lee branch cut as in Fig.1, the scaling functions come as complex conjugate pairs on both edges of branch cut. For example, we denote $\hat{M}_1(u \pm i0) = \hat{M}_1^{(\pm)}(u)$ when $u < -\xi_0^2$, and $(\hat{M}_1^{(+)*})^* = \hat{M}_1^{(-)}$.

minimal model $\mathcal{M}_{2,5}$ [8], usually referred to as the Yang-Lee conformal field theory (YLCFT). This CFT is non-unitary, with central charge $c_{2,5} = -\frac{22}{5}$.

Following the standard analyticity as in Fig.1, $\hat{M}_1(u)$ at any complex u can be expressed through the discontinuities across the Yang-Lee branch cut. On the Yang-Lee branch cut, $\text{Disc } \hat{M}_1(u) = 2i \Im \hat{M}_1(u)$, and we have

$$\hat{M}_1(u) = 1 + u \int_{\xi_0^2}^{\infty} \frac{dx \Im \hat{M}_1(-x + i0)}{\pi x(x+u)}, \quad (1.6)$$

which is known as the high-T mass dispersion relation [1]. Similar dispersion relations also can be formulated for some other scaling functions, see e.g. [9], or [2][4]. Additionally, the standard analyticity states that no other singularity exist along the YL branch cut, thus $\Im \hat{M}_1(u + i0)$ is a smooth function on the interval $-\infty < u \leq -\xi_0^2$. The behaviour of discontinuity near both ends ($u = -\xi_0^2$ and $u = -\infty$) are controlled by the expansions in $(u + \xi_0^2)$ or $\eta = u^{-\frac{4}{15}}$.

When u is close to $-u_0 := -\xi_0^2$, the Yang-Lee critical point serves as an infrared fixed point of renormalization group flow. The criticality are controlled by YLCFT, and the theory at infrared can be described by the effective action:

$$\mathcal{A}_{\text{eff}} = \mathcal{A}_{2,5}^* + \lambda(u) \int \phi(x) d^2x + \sum_i g_i(u) \int \mathcal{O}_i(x) d^2x, \quad (1.7)$$

where $\mathcal{A}_{2,5}^*$ is the action of YLCFT. $\phi(x)$ is the only nontrivial relevant scalar operator of minimal model $\mathcal{M}_{2,5}$, with normalization⁴:

$$\langle \phi(x) \phi(0) \rangle \rightarrow -|x|^{4/5}, \quad (1.8)$$

at $x \rightarrow 0$, and conformal dimensions $(\Delta_\phi, \bar{\Delta}_\phi) = (-\frac{1}{5}, -\frac{1}{5})$. $\lambda(u)$ is the associated relevant coupling with the mass dimension $[\lambda] = \frac{12}{5}$ ⁵. $\mathcal{O}_i(x)$ denote irrelevant scalar operators, which are scalar descendent operators in minimal model $\mathcal{M}_{2,5}$, and the corresponding couplings g_i 's have negative mass dimensions.

The effective action (1.7) is infrared asymptotically integrable, i.e. it is integrable if one drops all the irrelevant operators of (1.7). The theory with action:

$$\mathcal{A}_{\text{YLQFT}} = \mathcal{A}_{2,5}^* + \lambda \int \phi(x) d^2x \quad (1.9)$$

is known as Yang-Lee QFT, as the deformation of YLCFT with its only relevant nontrivial scalar operator $\phi(x)$. The Yang-Lee QFT is gapped and integrable, with the solvable elastic S-matrix [12]. But the effective description (1.7) is not integrable at any finite energy scale, since with nonvanishing g_i the generic irrelevant perturbations break the integrability⁶.

⁴In literature there are different choices of normalization, trading positivity norm of Hilbert space to real structure constant. By choosing the following $\phi(x)$, the structure constant $\mathbb{C}_{\phi\phi}^\phi$ is real. See e.g. [10][11][1].

⁵When $u > -\xi_0^2$, λ is positive, and the effective description has a unique vacuum.

⁶The exceptions which do not break integrability are the $T\bar{T}$ or $T\bar{T}$ -like operators [13], but any descendant of $\phi(x)$ would break integrability, see [1] for the analysis regarding $L_{-4}\bar{L}_{-4}\phi(x)$.

Denote the conformal dimension of the scalar $\mathcal{O}_i(x)$ as (Δ_i, Δ_i) , and the mass dimension of its coupling as $[g_i] = 2 - 2\Delta_i$. The couplings admit regular expansion in powers of $\Delta u = u + u_0$:

$$\lambda(u) = \lambda_1 \Delta u + \lambda_2 \Delta u^2 + \dots, \quad (1.10)$$

$$g_i(u) = g_i^{(0)} + g_i^{(1)} \Delta u + g_i^{(2)} \Delta u^2 + \dots. \quad (1.11)$$

By dimensional analysis, the leading critical behaviour of $\hat{M}_1(u)$ is $\hat{M}_1 \sim \lambda^{5/12} \sim (u + u_0)^{5/12}$, which is determined by the relevant operator $\phi(x)$. At $u > -u_0$, the leading critical amplitude is given by $\hat{M}_1/(u + u_0)^{5/12} \rightarrow b_0$ when approaching the Yang-Lee point. Beyond leading order, the form of subleading critical behaviors are also given by dimensional analysis:

$$\frac{\hat{M}_1(u)}{b_0(u + u_0)^{5/12}} = 1 + \sum_i C_i g_i(u) \hat{M}_{\text{YL}}(u)^{2\Delta_i - 2} + \sum_{ij} C_{ij} g_i(u) g_j(u) \hat{M}_{\text{YL}}(u)^{2\Delta_i + 2\Delta_j - 4} + \dots,$$

where $\hat{M}_{\text{YL}}(u) = C_{\text{YL}} \lambda(u)^{5/12}$ is the mass of Yang-Lee particle, where $C_{\text{YL}} = 2.6429\dots$ [14] is the coefficient of Yang-Lee mass-coupling relation. C_i and C_{ij} are dimensionless numbers given by corresponding matrix elements⁷. For example, the lowest irrelevant scalar operator is the famous $T\bar{T}$ operator, with conformal dimensions $(2, 2)$. As a result, the singular expansion of \hat{M}_1 reads:

$$\hat{M}_1(u) = (u + u_0)^{5/12} \left[b_0 + b_1(u + u_0) + c_0(u + u_0)^{5/6} + \dots \right]. \quad (1.12)$$

Here b_1 is related to λ_2 of (1.11), and c_0 is related to the leading $T\bar{T}$ coupling $g_{T\bar{T}}^{(0)}$. The critical amplitudes of (1.12) were measured in [1]. Below the Yang-Lee point with $u < -u_0$, analytic continuation of (1.12) gives the behaviour of discontinuity near the Yang-Lee point, which reads (with $u + u_0 < 0$):

$$\Im m \hat{M}_1(u + i0) = (-u - u_0)^{5/12} \left[b_0 \sin\left(\frac{5\pi}{12}\right) + b_1(-u - u_0) \sin\left(\frac{17\pi}{12}\right) + c_0(-u - u_0)^{5/6} \sin\left(\frac{5\pi}{4}\right) + \dots \right].$$

On the other hand, at $\xi = \infty$ or $\eta = 0$ the theory also becomes integrable, which is known as E_8 field theory due to its connection to E_8 algebra⁸. We call the point $\xi = \infty$ or $\eta = 0$ the E_8 point. Near the E_8 point at small η , IFT can be regarded as the perturbation of E_8 field theory with the relevant operator $\varepsilon(x)$, and the scaling functions are expandable as power series in $\eta = m/h^{8/15}$. For example, at $\eta \rightarrow 0^-$ or $u \rightarrow +\infty$:

$$\mathcal{M}_1(\eta) = \sum_{n=0}^{\infty} M_1^{(n)} \eta^n, \quad \text{and} \quad \hat{M}_1(u) = u^{4/15} \sum_{n=0}^{\infty} M_1^{(n)} u^{-4n/15}, \quad (1.13)$$

⁷The couplings C_{ij} and higher ones can not be determined via straightforward perturbation theory due to non-renormalizability, due to the presence of an infinite number of ambiguous counter terms. However, the general form of the expansion is fully determined by the dimensional analysis.

⁸When $m = 0$ with h is real and nonvanishing, this IFT is massive integrable with 8 stable particles. Their masses M_p with $p = 1, 2, \dots, 8$ are proportional to the components of Frobenius vector of E_8 Cartan matrix, and the scatterings of stable particles also reflect the properties of E_8 root system in various ways [15].

where the coefficients can be represented using the form factors of $\varepsilon(x)$ in E_8 field theory. The exact values of $M_1^{(0)}$ and $M_1^{(1)}$ were computed in the literature [16][17][18][19][1]. As a result, the behavior of discontinuity $\Im m \hat{M}_1(u + i0)$ at $u \rightarrow -\infty$ is given by the continuation of (1.13), as the expansion:

$$\Im m \hat{M}_1(u + i0) = u^{\frac{4}{15}} \sum_{n=0}^{\infty} M_1^{(n)} u^{-\frac{4n}{15}} \sin\left(\frac{4(1-n)}{15}\right). \quad (1.14)$$

Some properties of the low-T regime

In this subsection, we will briefly introduce the physical interpretations of IFT in the low-T phase. When $T < T_c$ with $h = 0$, the \mathbb{Z}_2 symmetry is broken by the nonvanishing spontaneous magnetization. Because of that, the low-T phase of $T < T_c$ is also known as the ordered phase. Ising model become the playground of more abundant interesting phenomena in the low-T phase, like confinement, nucleation and false vacuum decay. Some of them are reflected by the M_1 analyticity in low-T, and will be discussed in the following sections.

When $h = 0$, the vacua of low-T IFT are double degenerate. Denote the degenerate vacua as $|\pm\rangle$, they differ by the sign of spontaneous magnetizations, as:

$$\langle \pm | \sigma(x) | \pm \rangle = \pm \bar{\sigma} = \pm \bar{s} |m|^{\frac{1}{8}}, \quad \text{with} \quad \bar{s} = 2^{\frac{1}{12}} e^{-\frac{1}{8}} A_G^{3/2} = 1.35783834\dots, \quad (1.15)$$

where A_G is the Glaisher's constant [9]. The degeneracy of $|\pm\rangle$ vacua is lifted once a small nonvanishing h is presented. With small positive h , the interaction raises the energy density of $|+\rangle$, and lowers the one of $|-\rangle$. Thus $|-\rangle$ becomes the true stable vacuum, while $|+\rangle$ loses its stability and becomes the metastable vacuum. Similar to many other systems with slightly broken double degenerated vacua, fluctuations lead to the instability of metastable phase, and the decay/tunneling from the metastable vacuum to the true vacuum is described by the theory of nucleation. See [20][21] for systematic discussions.

In the low-T phase, analyticity of scaling functions are very different comparing to the ones of the high-T phase. Consider the scaling function of free energy density in low-T, which is defined as:

$$\mathcal{F}(\xi) = \frac{1}{|m|^2} \left(F(m, h) - \frac{m^2}{8\pi} \log m^2 \right), \quad (1.16)$$

where the second term is of subtracting Onsager's singularity [2]. $\mathcal{F}(\xi)$ is a single-valued continuous function on positive real axis of ξ , and is expandable as an asymptotic series in powers of ξ at small positive ξ . On the complex ξ -plane, the low-T analyticity of $\mathcal{F}(\xi)$ follows from the Yang-Lee theory of the low-T, see e.g. [2][21][22][23][24][25].

The low-T analyticity of function $\mathcal{F}(\xi)$ states that $\mathcal{F}(\xi)$ can be continued to a function of generic complex ξ . The function is analytic on the whole ξ -plane, except for $\xi = 0$ where a branching essential singularity is located. We call $\xi = 0$ the Fisher-Langer point. In [2], the associated Fisher-Langer's branch cut is chosen to be along the negative real ξ -axis, extending from $\xi = -\infty$ to $\xi \rightarrow 0^-$. This defines the principle branch of $\mathcal{F}(\xi)$ in the low-T regime. Along the Fisher-Langer's branch cut, $\mathcal{F}(\xi)$ has a nonvanishing discontinuity. The analytic

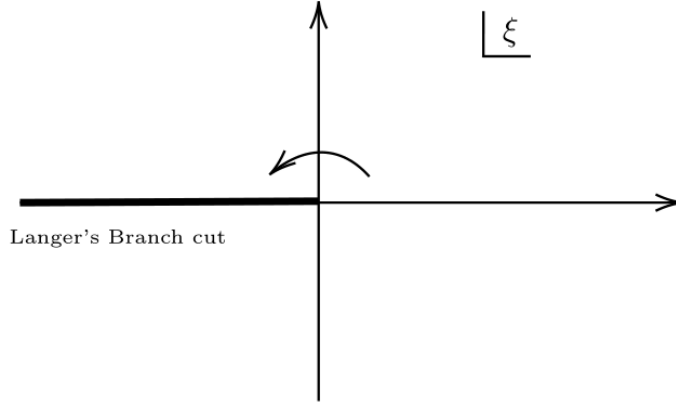


Figure 2. Phase diagram of $\mathcal{F}(\xi)$ on the complex ξ plane when $T < T_c$. Point $\xi = 0$ is the Fisher-Langer point, as a branching essential singularity. The branch cut extends along the negative real axis of ξ , which define the principle branch of $\mathcal{F}(\xi)$.

structure of $\mathcal{F}(\xi)$ is as shown in Fig.2. No other singularity exist either at other complex ξ or along the negative real ξ -axis.

The low-T analyticity is suggesting the associated dispersion relation, as representing the scaling function by an integration along the Fisher-Langer's branch cut. The discontinuity of $\mathcal{F}(\xi)$ on the branch cut is pure imaginary, as $\text{Disc } \mathcal{F}(\xi) = 2i\Im \mathcal{F}(\xi + i0)$ ⁹ with $\xi < 0$. The discontinuity $\text{Disc } \mathcal{F}(\xi)$ is controlled by its behaviours at both $\xi \rightarrow -\infty$ and $\xi \rightarrow 0^-$. Near the E_8 point $\xi \rightarrow +\infty$, similar to (1.13) but with positive η , \mathcal{F} can be expanded as integer powers of η , or equivalently of $\xi^{-\frac{8}{15}}$. The expansion can be safely continued as $\xi \rightarrow e^{\pm\pi i}\xi$ with sufficient large ξ , and would result in the expansions of $\Im \mathcal{F}(\xi + i0)$ at $\xi \rightarrow -\infty$.

However, the behaviour of $\mathcal{F}(\xi)$ become less regular near the essential singularity $\xi = 0$. For small positive ξ , $\mathcal{F}(\xi)$ is expandable in integer power series of ξ , as[2]:

$$\mathcal{F}(\xi) = -\bar{s}\xi + \tilde{G}_2\xi + \dots, \quad (1.17)$$

in the low-T regime. The continuation of (1.17) would find vanishing $\Im \mathcal{F}(\xi + i0)$ on the negative real axis, by using $\xi \rightarrow e^{\pm\pi i}\xi$. Instead, at $\xi \rightarrow 0^-$, $\Im \mathcal{F}(\xi + i0)$ is given by the theory of nucleation [20][21][26], as:

$$\Im \mathcal{F}(\xi + i0) \sim \frac{\lambda}{4\pi} e^{-\frac{\pi}{\lambda}}, \quad \text{where } \lambda = -2\bar{s}\xi > 0. \quad (1.18)$$

The expression (1.18), as the imaginary part of metastable free energy density, is related to the decay rate of metastable vacuum. See [21] for more details.

In [2], numerical approximation of $\Im \mathcal{F}(\xi + i0)$ was provided, based on the above analysis of $\xi \rightarrow -\infty$ and $\xi \rightarrow 0^-$ asymptotic expressions. The low-T dispersion relation of $\mathcal{F}(\xi)$ was

⁹At low-T, the relation $\mathcal{F}(\xi^*) = \mathcal{F}(\xi)^*$ still holds, and at real negative ξ the discontinuity is $\text{Disc } \mathcal{F}(\xi) = \mathcal{F}(\xi + i0) - \mathcal{F}(\xi - i0) = 2i\Im \mathcal{F}(\xi + i0)$.

verified numerically, supporting the low-T analyticity as in Fig.2. It's believed that other scaling functions exhibit similar analyticity, but the form of essential singularities (as (1.18)) would be different. The low-T analyticity of $\hat{M}_1(\xi)$ will be analyzed and numerical verified in Sec.2.

Spectrum in low-T domain

While any QFT in its Euclidean version can be interpreted as statistical mechanics of fields, the 1+1d Minkowskian version of IFT (1.1) gives rise to interesting relativistic particle theory. In the low-T domain with small ξ , the massive excitations of 1d Ising spin chain are interpreted as Ising mesons with tower-like meson spectrum. This serves as a result of the confining interaction from external magnetic field, and is known as the McCoy-Wu scenario [27][28][9].

At zero magnetic field h , the Ising action (1.1) can be reduced to the free fermion action:

$$\mathcal{A}_{\text{FF}} = \frac{1}{2\pi} \int d^2x (\psi \bar{\partial} \psi + \bar{\psi} \partial \bar{\psi} + im \bar{\psi} \psi), \quad (1.19)$$

where ψ and $\bar{\psi}$ denote the Majorana fermions. When $T < T_c$ and $h = 0$, the fermions can be understood as the domain walls separating regions filled with different degenerate vacua. When a small external magnetic field is presented, the vacua degeneracy is lifted, giving rise to a confining interaction between the fermions (which will be referred to as "quarks"). The interaction energy is proportional to the separation between two quarks, and the bound state can be interpreted as one string attaching with two quarks. The string tension is $f_0 = 2\bar{\sigma}h$ when h is small, and can be interpreted as difference of energy densities between stable and metastable vacuum. The bounded pairs of quarks would behave as mesons, just like other 2d confining models [29] but without color symmetry structure. As the result, the massive excitations of 2d low-T IFTs are understood roughly as the confined pairs of quarks. Under the 2-quark approximation, various methods can be applied to compute the approximated Ising meson spectrum.

In the non-relativistic limit, the hamiltonian of a single Ising meson involves of two quarks with a linear potential:

$$H = 2m + \frac{p_1^2 + p_2^2}{2m} + 2\bar{\sigma}h|x_1 - x_2|. \quad (1.20)$$

The non-relativistic mass spectrum is given by eigenvalues of (1.20), reads:

$$M_n \rightarrow 2m + m \left(\frac{2\bar{\sigma}h}{m^2} \right)^{\frac{2}{3}} z_n \quad \text{with} \quad \text{Ai}(-z_n) = 0, \quad (1.21)$$

where z_n label consecutive zeros of the Airy function $\text{Ai}(-z)$ [27, 28]. This approximation works well for $n \ll m^2/\bar{\sigma}h$. For higher-levels with $n \sim m^2/\bar{\sigma}h$, relativistic effects must be included, and what is called the semi-classical quantization is more suitable.

Consider a relativistic Ising meson consisting of two quarks. In the center of mass frame, the classical trajectories of both quarks moves back and forth periodically. The trajectories

look like lentils, with each quark draw part of a hyperbola in each period. Parameterizing the rapidities of quarks as $\pm\beta$, the classical trajectories are given by:

$$p = \frac{p_1 - p_2}{2} = -m \sinh \beta, \quad x = x_1 - x_2 = \frac{m}{\bar{\sigma}h} (\cosh \vartheta - \cosh \beta), \quad (1.22)$$

where ϑ is the maximum rapidity which occurs at quarks crossing. The action per period of the classical trajectory reads:

$$\oint p dx = \frac{m^2}{\bar{\sigma}h} \int_{-\vartheta}^{+\vartheta} \sinh^2 \beta d\beta = \frac{\sinh 2\vartheta - 2\vartheta}{\lambda}, \quad \text{with } \lambda = \frac{2\bar{\sigma}h}{m^2}, \quad (1.23)$$

which should be quantized. Quantization condition is given by the Bohr-Sommerfeld rule, as:

$$2 \oint p dx = 2\pi(N + \frac{1}{2}), \quad (1.24)$$

where N is a positive odd integer due to fermionic nature of quarks. By denoting $N = 2n - 1$, the quantization gives discrete ϑ_n and meson spectrum, as:

$$\sinh 2\vartheta_n - 2\vartheta_n = 2\pi\lambda(n - \frac{1}{4}), \quad M_n = 2m \cosh \vartheta_n, \quad (1.25)$$

with M_n is also called the WKB mass of meson. Higher order correction of (1.25) is available, as of the form:

$$\sinh 2\vartheta_n - 2\vartheta_n = 2\pi\lambda(n - \frac{1}{4}) - \lambda^2 \bar{S}_1(\theta) + O(\lambda^3), \quad M_n = 2m \cosh \vartheta_n, \quad (1.26)$$

with $\bar{S}_1(\theta)$ is a meromorphic function of θ , with explicit form given in [30][31].

A more systematic analysis of Ising meson spectrum using 2-quark approximation requires solving the corresponding Bethe-Salpeter equation [30]. The Bethe-Salpeter equation is derived using the known matrix elements $\langle q(\theta)q(-\theta) | \sigma(0) | q(\theta')q(-\theta') \rangle$. The details of [30] is too lengthy to be introduced here, but we would collect the useful conclusions. At small positive λ , the Ising meson masses admit the expansion (see also [31]):

$$M_n(m, h) = 2m + m \sum_{k=1}^{\infty} c_n^{(k)} \lambda^{\frac{2k}{3}} + m \sum_{l=4}^{\infty} d_n^{(l)} \lambda^{\frac{2l+1}{3}}. \quad (1.27)$$

Roughly speaking, M_n can be expanded as an asymptotic series of $\lambda^{\frac{2}{3}}$, plus corrections of power series of $\lambda^{\frac{1}{3}}$ starting from relatively higher orders. Some coefficients of (1.27) were computed in [30], while the non-relativistic spectrum (1.21) and WKB spectrum (1.25) approximate well the leading coefficients $c_n^{(k)}$ in (1.27).

Although all the above methods give good approximations of the Ising meson spectrum, they cannot explain the decay of heavier mesons and the inelastic scattering processes, because these phenomena include multi-quark effects. For any meson with mass $M_n > 2M_1$, the decay channel into two lightest meson opens, and the n -th meson is no longer stable. The 2-quark

approximations become less accurate when M_n approaches $2M_1$. We would instead denote the stable mesons as M_p with $p = 1, 2, 3, \dots, P$. The number of stable mesons P decreases with growing ξ . In the strong coupling limit $\xi \rightarrow +\infty$ or $\eta \rightarrow 0^+$, the Ising field theory can be regarded as perturbed E_8 field theory. At sufficiently large ξ , only $M_{1,2,3}$ are below the stability threshold $2M_1$, and other higher mesons cross their stability thresholds at finite values of ξ 's. The analyticity of higher meson masses is an interesting questions, and we plan to address it elsewhere.

Remarks

Similar to the previous works [1-4], this paper is a combination of both analytic computations and numerical analysis. With the same manner, the numerical data of Ising spectrum which are used in this work was obtained via Truncated Free Fermion Space Approach (TFFSA), and the details of TFFSA were well discussed in [2] and [1]. For a given ξ (or η), TFFSA is able to numerically compute the energy levels $E_n(R)$ of IFT on a cylinder with good accuracy¹⁰ (here we denote circumference of the cylinder as R). At large R , the energy gaps $\Delta E_n(R) = E_n(R) - E_0(R)$ approach some constants M_n exponentially, which are identified as the energies of particle states. In this work, we use the same set of $\mathcal{M}_p(\eta)$ or \hat{M}_p data as in [3] and [1]. The behaviour of $\mathcal{M}_{1,2,3}$ near $\eta = 0$ are as plotted in Fig.3, and the details of data measurements are omitted here.

In Sec.2, we propose the low-T analyticity conjecture of the stable particle masses $M_{1,2,3}$, with the associated low-T dispersion relations are given in (2.10). The low-T analyticities are checked in this section numerically, as is shown in Fig.6 and (2.14). In Sec.3, we turn to the complex η -plane and propose the extended analyticity conjecture of the lowest mass M_1 . The extended dispersion relation is given as (3.8), and the extended analyticity of M_1 is numerically verified in various ways. Finally, in Appendix B, we give a detailed analysis on the "instanton-like" terms, which come from the tunneling between the degeneracy-lifted vacua. These "instanton-like" terms are small enough to be negligible in the discussion of Sec.2 and Sec.3. In Appendix A, we cover some technical details of constructing the discontinuities for the extended dispersion relation (3.8).

2 Analyticity of $\hat{M}_p(\xi)$, $p = 1, 2, 3$ and the Fisher-Langer's branch cut

In the low-T phase with $T < T_c$ (or $m > 0$), IFT has at least three stable particles, with their masses denoted as M_p , $p = 1, 2, 3$. Here we focus on the analytic properties of the associated scaling functions $\hat{M}_p(\xi) = M_p(m, h)/|m|$ on the complex ξ -plane. For any $p \geq 4$, the corresponding Ising meson becomes unstable at sufficiently large ξ (or small positive η), making its analyticity more complicated. For the stable mesons $p = 1, 2, 3$ one expects that the functions $\hat{M}_p(\xi)$, being analytically continued from the positive part of the real ξ -axis, are analytic on the whole complex ξ -plane, except at the Fisher-Langer essential singularity at

¹⁰Usually 5 to 6 digits when not close to any critical point.

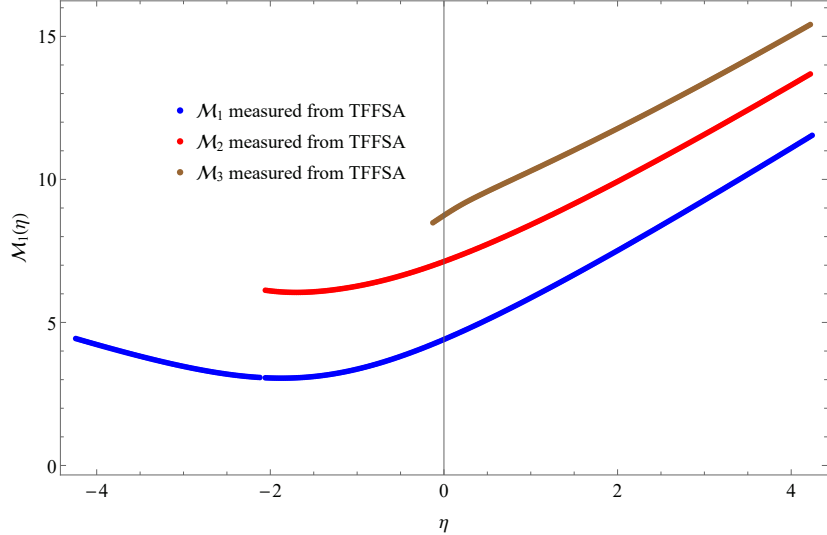


Figure 3. The spectrum of scaling function $\mathcal{M}_p(\eta)$ with $p = 1, 2, 3$ near $\eta = 0$, which represent the masses of three lightest particle. The numerical data was obtained using the truncated free fermion space approach (TFFSA). We are using the same set of data as in [3] and [1].

$\xi = 0$, and the associated Fisher-Langer branch cut; the latter extends along the negative part of the real axis, from $-\infty$ to 0. Under this assumption the $M_p(\xi)$ can be expressed through the discontinuity across this branch cut via the corresponding dispersion integral.

Analytic continuation of M_p

At small ξ the functions $\hat{M}_p(\xi)$ admit the asymptotic expansion (1.27), with $\lambda = 2\bar{s}\xi$. On the other hand, when $\xi \gg 1$ the IFT can be regarded as E_8 field theory perturbed by the energy density operator $\varepsilon(x)$, and the scaling functions $\mathcal{M}_p(\eta)$ enjoy regular expansions

$$\mathcal{M}_p(\eta) = \frac{M_p(m, h)}{|\hbar|^{8/15}} = M_p^{(0)} + M_p^{(1)}\eta + M_p^{(2)}\eta^2 + M_p^{(3)}\eta^3 + \dots, \quad (2.1)$$

which converge at sufficiently small η . Equivalently, on the complex ξ -plane the expansion (2.1) reads

$$\hat{M}_p(\xi) = \frac{M_p(m, h)}{|m|} = \xi^{\frac{8}{15}} \left(M_p^{(0)} + M_p^{(1)}\xi^{-\frac{8}{15}} + M_p^{(2)}\xi^{-\frac{16}{15}} + M_p^{(3)}\xi^{-\frac{24}{15}} + \dots \right). \quad (2.2)$$

Some of the leading coefficients of (2.1) can be computed via the form-factor perturbation theory [16][17][18][19][1]. For example, $M_1^{(0)}$ is available from the mass-coupling relation of E_8 field theory, and $M_1^{(1)}$ was computed using the 2-point form-factor of $\varepsilon(x)$ operator [17]. The coefficients $M_2^{(0)}$ and $M_3^{(0)}$ follow straightforwardly from E_8 mass ratios [15],

$$M_2^{(0)}/M_1^{(0)} = 2 \cos \frac{\pi}{5}, \quad \text{and} \quad M_3^{(0)}/M_1^{(0)} = 2 \cos \frac{\pi}{30}. \quad (2.3)$$

The coefficients of $M_2^{(1)}$ and $M_3^{(1)}$ can also be computed by using the form factors of the E_8 field theory [17]. For higher coefficients, only numerical results are available. We list some of them in Tab.1, as well as numerical values of exact results from [17].

As is shown in Fig.2, the Fisher-Langer branch cuts of $\hat{M}_p(\xi)$ extends along the real negative ξ -axis. The discontinuities of $\hat{M}_p(\xi)$ across the branch cut are pure imaginary,

$$\text{Disc } \hat{M}_p(x) := \hat{M}_p(x + i0) - \hat{M}_p(x - i0) = 2i \Im m \hat{M}_p(x + i0), \quad (2.4)$$

where $x = -\xi > 0$. At sufficiently large positive x they enjoy the convergent expansions

$$\Im m \hat{M}_p(x + i0) = x^{\frac{8}{15}} \sum_{n=0}^{\infty} M_p^{(n)} \sin \left[\frac{8\pi(1-n)}{15} \right] x^{-\frac{8n}{15}}, \quad (2.5)$$

which follows from the term-by-term continuation of (2.2).

On the other hand, at sufficiently small ξ the same discontinuity (2.4) admits asymptotic expansion

$$\text{Disc } \hat{M}_p(x) = 2i \Theta(x) \left(\sum_{k=1}^{\infty} \hat{c}_p^{(k)} x^{\frac{2k}{3}} + \sum_{l=4}^{\infty} \hat{d}_p^{(l)} x^{\frac{2l+1}{3}} \right), \quad (2.6)$$

which follows from the continuation of (1.27), with $\Theta(x)$ is the step function. Here the coefficients are:

$$\hat{c}_p^{(k)} = (2\bar{s})^{\frac{2k}{3}} c_p^{(k)} \sin\left(\frac{2\pi k}{3}\right), \quad \text{and} \quad \hat{d}_p^{(l)} = (2\bar{s})^{\frac{2l+1}{3}} d_p^{(l)} \sin\left(\frac{\pi(2l+1)}{3}\right).$$

While few terms of this expansions approximate well the desired discontinuities only at very small x , at larger x the approximative power of these expansions is expected to deteriorate rapidly, not to mention that only limited number of the terms are available explicitly [30][31]. Instead, the leading semiclassical approximation (1.25) gives reasonably accurate results for $\hat{M}_p(\xi)$ at positive real ξ , for all but very large $\xi \gtrsim 2.0$ [30]. Thus, we will make an assumption (confirmed by the result of this Section) that analytic continuation of (1.25) to complex values of λ , including the negative part of the real axis, gives comparably accurate approximation of $\hat{M}_p(\xi)$ at all complex ξ with $|\arg(\xi)| \leq \pi$, as long as $|\xi| \lesssim 0.5$.

Below I will build an approximation for $\Im m \hat{M}_p(x)$, by combining the analytic continuation of the leading semiclassical spectrum (1.25) with the partial sums of the series (2.5). For every $p = 1, 2, 3$, the four leading terms of (2.5) match well with the analytic continuation of (1.25) at $|\xi| \simeq x_p^{\text{Int}}$,

$$x_1^{\text{Int.}} \approx 0.369927, \quad x_2^{\text{Int.}} \approx 0.469173, \quad x_3^{\text{Int.}} \approx 0.247037. \quad (2.7)$$

Then, we simply approximate $\text{Disc } \hat{M}_p(-\xi)$ with the four terms truncation of (2.5) when $\xi \leq -x_p^{\text{Int}}$, while using the analytic continuation of (1.25) for $0 > \xi > -x_p^{\text{Int}}$. The approximated discontinuities for $p = 1, 2, 3$ are as shown in Fig.5.

Here we shall explain how the analytic continuation of (1.25) is obtained. The quantization condition (1.25) has the form

$$\sinh 2\theta(t) - 2\theta(t) = t, \quad (2.8)$$

where we have consider t , once as discrete values in (1.25), now as a continuous parameter, and study the behavior of the solution $\theta(t)$. At given real and positive t , there exist three solutions, one is real (denoted as $\theta_0(t)$) and two are complex (denoted as $\theta_+(t)$ and $\theta_-(t)$). At real t the two complex solutions $\theta_+(t)$ and $\theta_-(t)$ are complex conjugate to each other. It is the real solution $\theta_0(t)$ which is taken in the quantization of the meson mass spectrum, but it is instructive to follow all the three families. At small t all three solutions behave as the three cubic root of t , while at large t the pair of solutions $\theta_+(t)$ and $\theta_-(t)$ monotonically approach $-\infty \pm \frac{\pi}{2}i$, as shown in Fig.4.

Now, let's make the parameter t complex, as writing $t \rightarrow e^{i\phi}|t|$ with some phase ϕ . When the phase ϕ increases the pattern of solutions changes as follows. At small t it just rotates by the angle $\phi/3$, while at large t the asymptotics of solutions $\theta_0(t)$ and θ_{\pm} generally changes. More precisely, when ϕ increases from zero to $\pi/2$, the solution $\Re \theta_0(t) \rightarrow +\infty$ and $\Re \theta_{\pm}(t) \rightarrow -\infty$ as $|t| \rightarrow \infty$, while their imaginary parts monotonically increase/decrease. At $\phi = \pi/2$ the solution $\theta_-(t)$ becomes pure imaginary at all $|t|$, extending along the negative part of imaginary axis. The two other solutions behave as $\theta_+ = -\Re \theta_0 + i \Im \theta_0$, and are as shown in Fig.4. When ϕ further increases from $\pi/2$ to π the solutions keep "rotating" counterclockwise, while preserving the signs of their real parts. Until at $\phi = +\pi$ the solution $\theta_+(t)$ becomes real negative, and $\theta_-(t)$ becomes complex conjugate of $\theta_0(t)$. Therefore, at $\xi < -x_p^{\text{Int}}$ we take

$$\begin{aligned} \text{Disc } \hat{M}_p(\xi) &:= \hat{M}_p(\xi + i0) - \hat{M}_p(\xi - i0) = 2i \Im \hat{M}_p(\xi + i0) \\ &\approx \Theta(-\xi) [2 \cosh \theta_+(-t) - 2 \cosh \theta_-(-t)] = 4i\Theta(-\xi) \Im (\cosh \theta_+(-t)), \end{aligned} \quad (2.9)$$

where $\Theta(x)$ is the step function, and t in the last expression is to be set to $4\pi\bar{s}\xi(p-1/4)$. This provides an leading semiclassical approximation for the discontinuity, which is expected to work well at sufficiently small $|\xi|$.

It is fair to note that the above approximation ignores possible "instanton-like" contributions to (2.4), which are exponentially small at $x \ll 1$ but may become significant at larger x . However, as will be argued in Appendix B, these contributions are numerically very small as compared to the above approximation, and disregarding them is legitimate.

The low-T dispersion relations for M_1 , M_2 and M_3 .

The low-T analyticity conjecture for M_1 , M_2 and M_3 states that: the associated scaling functions $\hat{M}_1(\xi)$, $\hat{M}_2(\xi)$, $\hat{M}_3(\xi)$ are analytic in the whole complex ξ -plane, with the Fisher-Langer branch cut extending along the real axis from $-\infty$ to 0, as is depicted in Fig.2. The discontinuities $\text{Disc } \hat{M}_p(-x) = 2i\Im \hat{M}_p(-x + i0)$ are pure imaginary continuous functions at $x > 0$. Under this conjecture the following dispersion relations hold,

$$\hat{M}_p(\xi) = 2 + \xi \int_0^{+\infty} \frac{dx}{\pi} \frac{\Im \hat{M}_p(-x + i0)}{x(x + \xi)}, \quad (2.10)$$

for all complex ξ in Fig.2. For the function $\mathcal{M}_p(\eta) = \eta \hat{M}_p(\xi = \eta^{15/8})$ these relations take the form

$$\mathcal{M}_p(\eta) = 2\eta + \frac{15\eta}{8\pi} \int_0^\infty dz \frac{z^{7/8} \Im m \hat{M}_p(-z^{-15/8} + i0)}{z^{15/8} + \eta^{15/8}}. \quad (2.11)$$

Under the above low-T analyticity conjecture, this dispersion relation holds as long as $|\arg \eta| \leq 8\pi/15$. Below the certain approximations for $\Im m \hat{M}_p(-x+i0)$ are proposed, and the dispersion relation (2.11) are verified numerically.

At large ξ , $\Im m \hat{M}_p(-x+i0)$ can be approximated by few leading terms of the expansion (2.5). Two leading coefficients of this expansion are known exactly from form factor perturbation theory [17], and two more can be extracted from the TFFSA for $\mathcal{M}_p(\eta)$. These coefficients are presented in Table 1. On the other hand, at small $|\xi|$ the leading semiclassical formula (2.9) provides good approximation. Simultaneous plots of four leading terms of the expansion (2.5) and the semiclassical approximation (2.9) are presented in Fig.5 for $p = 1, 2, 3$. The plot of the estimate (B.33) of the "instanton-like" contribution is also shown in this Figure, where one can see that the latter contribution is negligible. One can also observe that the above

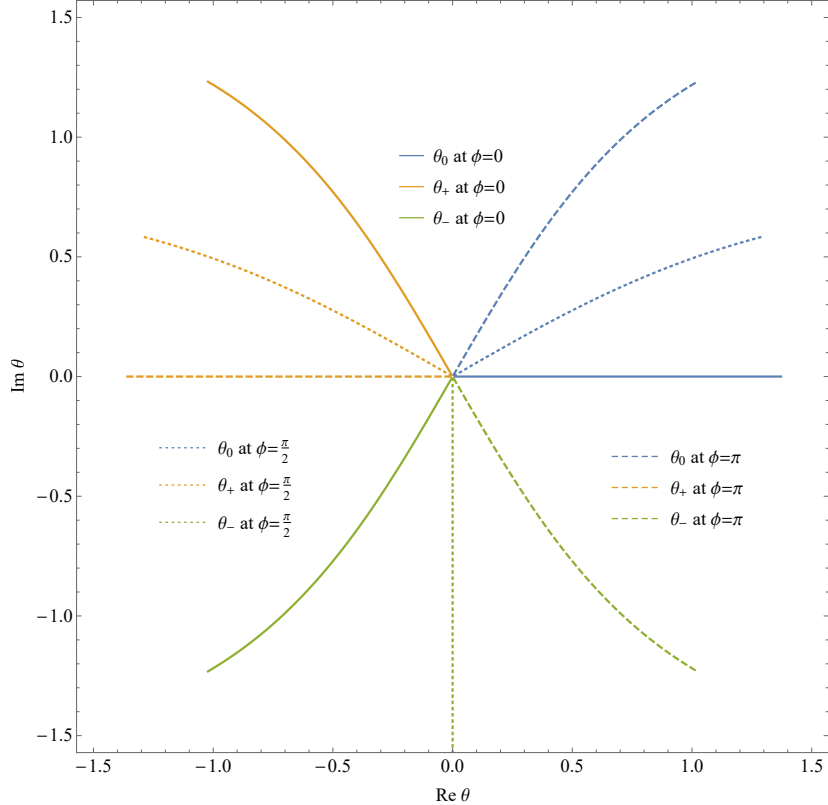


Figure 4. The evolution of solutions to the transcendental equation (2.8), along with the phase angle $\phi = \text{Arg } t$ varies from 0 to π . Three solutions of (2.8), namely θ_0 , θ_+ and θ_- , are given by curves in different colors. Each of them rotates counterclockwisely near the origin.

$M_1^{(0)}$	$M_1^{(1)}$	$M_1^{(2)}$	$M_1^{(3)}$
4.405	1.295	0.2002	-0.051
$M_2^{(0)}$	$M_2^{(1)}$	$M_2^{(2)}$	$M_2^{(3)}$
7.130	1.113	0.2116	-0.040
$M_3^{(0)}$	$M_3^{(1)}$	$M_3^{(2)}$	$M_3^{(3)}$
8.740	1.978	-0.3804	-1.0

Table 1. Coefficients of $\mathcal{M}_p(\eta)$ expansions (2.1) near $\eta = 0$. Among the coefficients $M_p^{(k)}$, $M_p^{(0)}$ & $M_p^{(1)}$ were computed using form factor perturbation theory [16][17][18][19][1], while $M_p^{(2)}$ and $M_p^{(3)}$ were measured from the spectrum data [3][1][4].

large ξ and small ξ approximations match at some intermediate values of $\xi = -x_p^{\text{Int}}$, shown above in (2.7). Therefore, for each $p = 1, 2, 3$, we propose the approximation

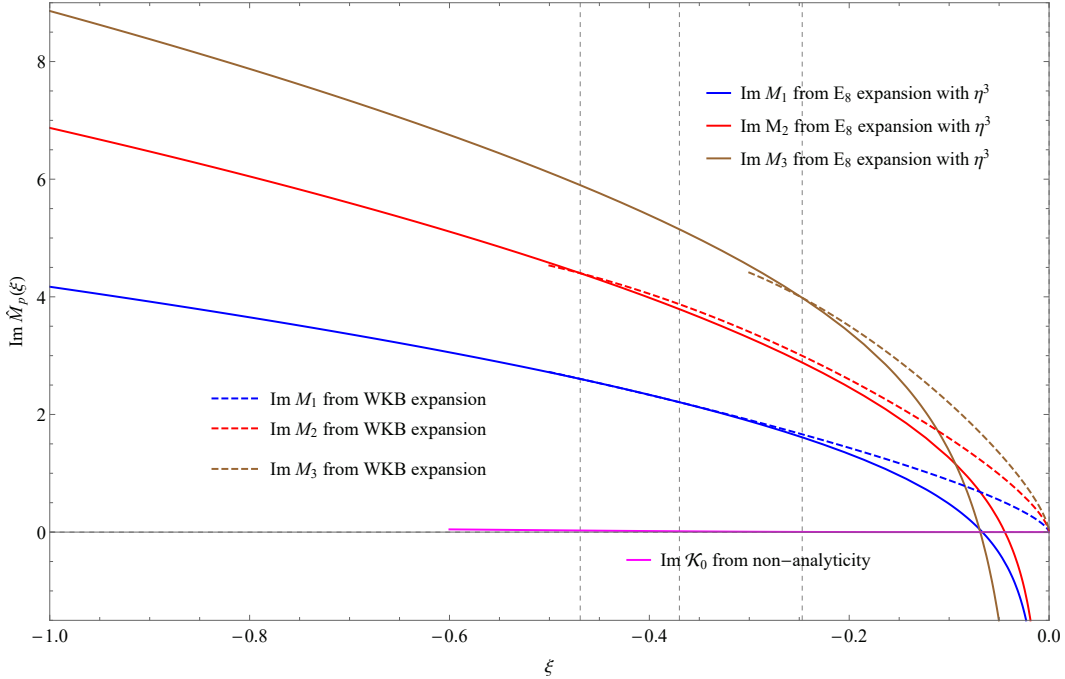


Figure 5. Matching the functions $\Im m \hat{M}_p(\xi + i0)$ for $\xi < 0$, as illustrate the behaviours of the discontinuities (2.4) along the Fisher-Langer’s branch cut. In this plot, blue, red and brown solid curves are showing $\Im m \hat{M}_p(\xi + i0)$ with $p = 1, 2, 3$ following the expansions (2.5), which works for $\xi \rightarrow -\infty$. The coefficients $M_p^{(k)}$ of (2.5) are those of Tab.1, and the series are truncated till the terms with $M_p^{(3)}$. On the other hand, blue, red and brown dashed curves are illustrating the continuation of semiclassical quantization spectrum, see (2.9) and the related discussion. The curves of the same color match at different $\xi = -x_p^{\text{Int}}$, with the values given in (2.7). Lastly, the magenta curve is the instanton-like term $\Im m \mathcal{K}_0$ (B.34), which is almost negligible comparing to other contributions, thus omitted in the dispersion integral (2.10).

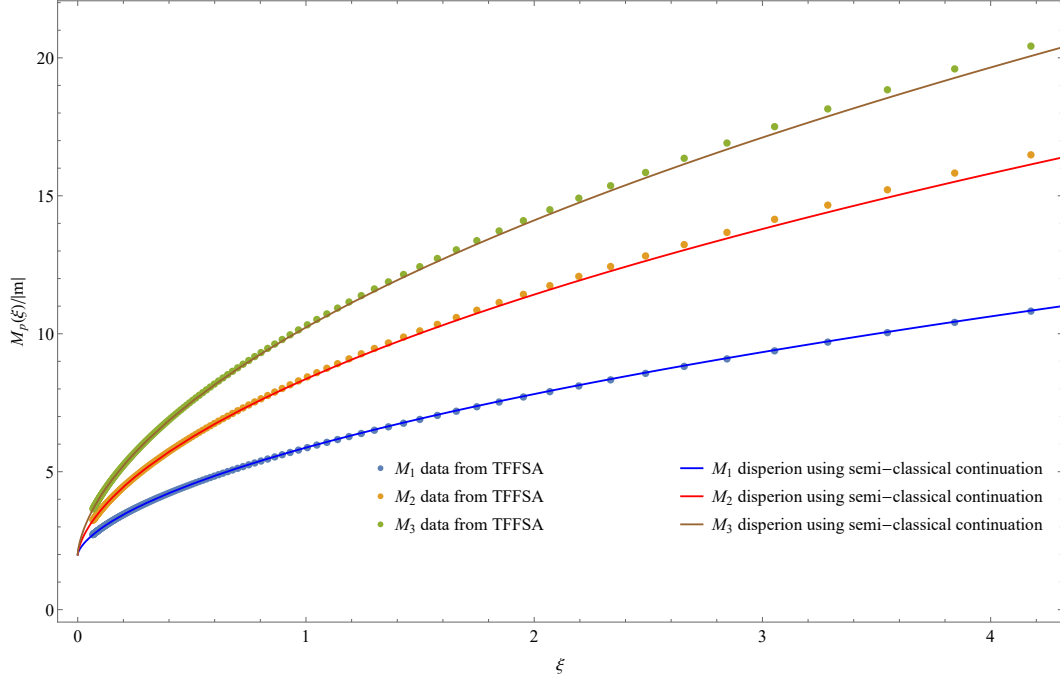


Figure 6. The verifications low-T dispersion relations (2.10) with $p = 1, 2, 3$ by numerical integrations. The discontinuities (2.4) of the integration are approximated using (2.12), namely using (2.5) for $\xi < -x_p^{\text{Int}}$ and (2.9) for $\xi > -x_p^{\text{Int}}$. The results of numerical integrations are as solid curves, which are to be compared to the mass spectrum from TFFSA, as in Fig.3, with transformed from $\mathcal{M}_p(\eta)$ to $\hat{M}_p(\xi)$ (3.1). All three levels are showing good match between the dispersion integrals and measured data, supporting the low-T analyticity conjecture.

$$\text{Disc } \hat{M}_p^{\text{approx}}(-x) = \begin{cases} \text{Eq.(2.6) truncated to } n = 3 \text{ for } x > x_p^{\text{Int}}. \\ \text{Eq.(2.9)} & \text{for } x < x_p^{\text{Int}}. \end{cases} \quad (2.12)$$

With this approximation the dispersion integral in (2.11) can be evaluated numerically, and compared to the $\hat{M}_p(\xi)$ obtained from the TFFSA data. This comparison is shown in Fig.6. The close match supports our low-T analyticity conjecture.

Another independent verification can be made as follows. One notes that the approximation (2.12) does not involve any information of the coefficients $M_p^{(1)}$, since in (2.5) the term $\sim x^{-8/15}$ enters with vanishing coefficient. The dispersion relation allows one to restore this coefficient. Expanding (2.11) at large η one obtains

$$M_p^{(1)} = 2 + \frac{15}{8\pi} \int_0^\infty dz \left[\frac{\Im m \hat{M}_p(-z^{-15/8} + i0)}{z} - \frac{M_p^{(0)} \sin(\frac{8\pi}{15})}{z^2} \right], \quad (2.13)$$

Numerical evaluation of this integral with the approximation (2.12), we have

$$M_1^{(1)} \Big|_{\text{disp}} = 1.262, \quad M_2^{(1)} \Big|_{\text{disp}} = 1.084, \quad M_3^{(1)} \Big|_{\text{disp}} = 1.541, \quad (2.14)$$

which are to be compared with the exact values in Tab.1. One can see that these values deviate from the exact coefficients by 3% for $M_1^{(1)}$ and $M_2^{(1)}$ to 30% for $M_3^{(1)}$. This results are at least compatible with the low-T analyticity conjecture, but also show that our approximation for the discontinuity (2.12) while qualitatively correct but needs further refinement. We leave this question for further analysis.

3 Extended dispersion relation of M_1

The analyticity properties of scaling function $\hat{M}_1(\xi)$ in high-T regime and low-T regime have been discussed separately in [1] and Sec.2, and in this section, we will sew both together by considering the analyticity in terms of the scaling parameter η . We will turn to the analyticity of the function $\mathcal{M}_1(\eta)$, which is defined as (3.1) below. Specifically, we propose " M_1 extended analyticity " in this section, and support it by verifying numerically the associated dispersion relation.

$\mathcal{M}_1(\eta)$ on the complex plane of η

At real m and positive h , $\mathcal{M}_1(\eta)$ is defined as follows:

$$\mathcal{M}_1(\eta) = \frac{M_1(m, h)}{h^{\frac{8}{15}}} = \begin{cases} -\eta \hat{M}_1(\xi^2 = (-\eta)^{-\frac{15}{4}}) & \text{High-T: } \eta < 0 \\ +\eta \hat{M}_1(\xi = \eta^{-\frac{15}{8}}) & \text{Low-T: } \eta > 0 \end{cases}, \quad (3.1)$$

which is the lightest mass M_1 measured in the unit of $h^{\frac{8}{15}}$. (3.1) also illustrated how $\mathcal{M}_1(\eta)$ is related to the functions \hat{M}_1 of high-T and low-T regimes, differs by the sign of η . Furthermore, when $m < 0$ ($T > T_c$) and h is a pure imaginary, η becomes complex with $\text{Arg } \eta = \pm \frac{11\pi}{15}$, and $\mathcal{M}_1(\eta)$ becomes a complex function. By denoting $\eta = -ye^{\mp \frac{4\pi i}{15}}$, the scaling function $\hat{\mathcal{M}}_1(y) = |\mathcal{M}_1(\eta)|$ with $y > 0$ is related to $\hat{M}_1(\xi^2)$ of high-T by:

$$\hat{\mathcal{M}}_1(y) = |\mathcal{M}_1(\eta = -ye^{\mp \frac{4\pi i}{15}})| = e^{\pm \frac{4\pi i}{15}} \mathcal{M}_1(\eta = -ye^{\mp \frac{4\pi i}{15}}) = y \hat{M}_1(\xi^2 = -y^{-\frac{15}{4}}). \quad (3.2)$$

In Fig.1, $\hat{M}_1(\xi^2)$ is a single-valued function for $-\xi_0^2 \leq \xi^2 < 0$, thus (3.2) works for $y \geq Y_0$. As was discussed in [1] and Sec.2, $\mathcal{M}_1(\eta)$ was measured at real η and real y with good accuracy¹¹, by using the finite size spectrum from TFFSA (see e.g. [32] and [1]). These numerical data will be used in the following analysis, see e.g. Fig.9 and Fig.10.

At generic complex η , $\mathcal{M}_1(\eta)$ can be reached by continuing (3.1) from the real η -axis. On the complex η -plane, the first sheets of function $\hat{M}_1(\xi)$ for low-T and $\hat{M}_1(\xi^2)$ of high-T are mapped to different wedges [2]. The ξ -plane of $\hat{M}_1(\xi)$ for low-T, as was illustrated in Fig.2, is mapped to the wedge $|\text{Arg } \eta| < \frac{8}{15}\pi$. We call this wedge the low-T wedge (LTW). The boundaries of the low-T wedge are the rays $\text{Arg } \eta = \pm \frac{8}{15}\pi$, which are the images of upper/lower edges of the Fisher-Langer's branch cut (see Fig.2). LTW is further decomposed

¹¹For any real η or generic $y > Y_0$, the fitting procedure in [1] yields accuracy of 3 to 5 significant digits of \hat{M}_1 . When y becomes very close to Y_0 the Yang-Lee point, due to the large correlation length, the accuracy of \hat{M}_1 falls into 2 digits.

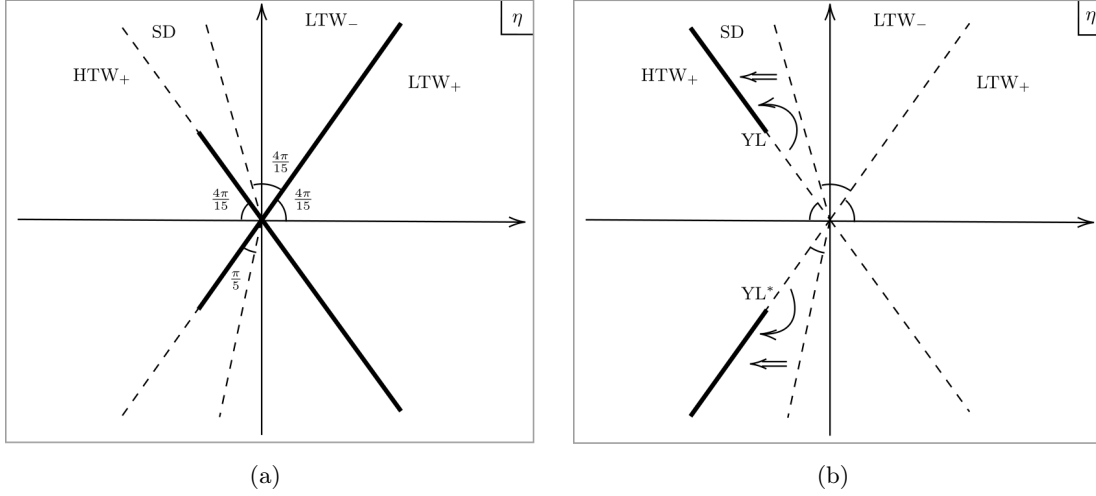


Figure 7. The analyticity structure of $\mathcal{M}_1(\eta)$ on the complex η -plane, with different choices of Yang-Lee branch cut and primary branches of $\mathcal{M}_1(\eta)$. $|\text{Arg } \eta| \leq \frac{8\pi}{15}$ is the low-T wedge (LTW), $|\text{Arg } (-\eta)| \leq \frac{4\pi}{15}$ is the high-T wedge (HTW) and $\frac{8\pi}{15} \leq |\text{Arg } \eta| \leq \frac{11\pi}{15}$ is the shadow domain (SD). The edges of Fisher-Langer's branch cut become the rays $\text{Arg } \eta = \pm \frac{8\pi}{15}$. (a): Mapping the high-T complex $u = \xi^2$ plane Fig.1 to the complex η -plane with $\eta = -u^{-4/18}$. Along the ray $\eta = -ye^{\mp \frac{4\pi i}{15}}$, the Yang-Lee branch cut extends from $y = Y_0$ to $y = -\infty$. (b): After the rotation of the Yang-Lee branch cut, it becomes extending from $y = Y_0$ to $y = +\infty$. This defines the principle branch of $\mathcal{M}_1(\eta)$. Now LTW and SD are compatible with HTW on the same complex η plane. The statement of extended analyticity is regarding analytic structure of SD, as there exist no singularities within the shadow domain or along the rotated Yang-Lee branch cut.

into the two domains, as LTW_+ for $|\text{Arg } \eta| < \frac{4}{15}\pi$, which was mapped from $\Re \xi > 0$, and LTW_- for $\frac{4}{15}\pi < |\text{Arg } \eta| < \frac{8}{15}\pi$, which was mapped from $\Re \xi < 0$. The LTW is as shown on the right half η -plane of Fig.7(a) and Fig.7(b).

When $T > T_c$, the image of complex ξ^2 -plane (see Fig.1) is the wedge $|\text{Arg } (-\eta)| < \frac{4}{15}\pi$, which is called the high-T wedge (HTW). The function $\mathcal{M}_1(\eta)$ in the HTW was mapped from $\hat{\mathcal{M}}_1(\xi^2)$ on the first sheet of complex ξ^2 -plane, as is shown in Fig.7(a). The negative real axis of ξ^2 -plane represents IFT with pure imaginary magnetic field, and its upper and lower edges mapped to the rays $\text{Arg } \eta = \pm \frac{11}{15}\pi$. On the complex η -plane, the Yang-Lee singularities are located at $\eta = -Y_0 e^{\mp \frac{4\pi i}{15}}$, which serve as branching points of scaling functions. As is shown in Fig.7(a), the choice of Yang-Lee branch cut in Fig.1 is mapped to $y \leq Y_0$ on the complex η -plane, along the rays $\eta = -ye^{\mp \frac{4\pi i}{15}}$.

However, the mapping of Fig.7(a) separates high-T wedge and low-T wedge in different isolated domains. From low-T point of view, the high-T ξ^2 -plane of Fig.1 is mapped to certain domain under the branch cuts in Fig.7(a). It can be exposed by rotating the branch cuts as shown in Fig.7(b). From high-T wedge point of view, the rotation of branch cuts is equivalent to redefine $\mathcal{M}_1(\eta)$ for $|\text{Arg } \eta| < \frac{11}{15}\pi$, in order to match the function $\mathcal{M}_1(\eta)$ of the low-T wedge. The function $\mathcal{M}_1(\eta)$ in the high-T wedge remains intact. Both LTW (including

LTW₊ & LTW₋) and HTW can now be embedded on the same η -plane, as shown in Fig.7(b). However, the complex η -plane is not fully covered by these wedges. The uncovered domain, namely $\frac{8}{15}\pi < |\text{Arg } \eta| < \frac{11}{15}\pi$, is called shadow domain (SD). From the low-T point of view, the shadow domain is on the second sheet of Fig.2, as behind the Fisher-Langer's branch cut. The shadow domain does not correspond to any physically well defined system.

After the rotation of branch cuts, the function $\mathcal{M}_1(\eta)$ becomes single-valued function on the rays $\text{Arg } \eta = \frac{11}{15}\pi$, for $0 < y \leq Y_0$. (3.2) now becomes:

$$\mathcal{M}_1(\eta = -ye^{\mp\frac{4\pi i}{15}}) = ye^{\mp\frac{4\pi i}{15}} \hat{M}_1(\xi^2 = -y^{-\frac{15}{4}} \pm i0). \quad (3.3)$$

For $y \geq Y_0$, the discontinuities of scaling functions across the Yang-Lee branch cut of Fig.7(b) are different. On the lower edge $\eta = -ye^{\mp(\frac{4\pi i}{15} + i0)}$, the function $\mathcal{M}_1(\eta)$ follows its behaviours in the HTW. While differently on the upper edge $\eta = -ye^{\mp(\frac{4\pi i}{15} - i0)}$, the function $\mathcal{M}_1(\eta)$ sits on the edges of the shadow domain, and can be reached by the continuation from the low-T wedge. The continuation corresponds to entering the second sheet of Fig.2, which is behind the Fisher-Langer's branch cut. Certain analytical structure in the shadow domain would affect the continuation. As a result, the analyticity of function $\mathcal{M}_1(\eta)$ on the complex η -plane is completely determined by its discontinuities along the rotated Yang-Lee branch cut, and the analytic structures in the shadow domain, as illustrated in Fig.7(b).

The M_1 extended analyticity conjecture, and its dispersion relation

The minimal assumption of $\mathcal{M}_1(\eta)$ analyticity is similar to the extended analyticity conjecture in [2], which states that on the first sheet of η -plane (see Fig.7(b)), the only singularities of the scaling function are the Yang-Lee branching points. In other words, no other singularities exist either within the shadow domain or on the rotated Yang-Lee branch cut. The Yang-Lee branching points are the closest non-trivial singularities behind the Fisher-Langer's branch cut. We call this analyticity statement of $\mathcal{M}_1(\eta)$ as M_1 extended analyticity conjecture. On the rotated Yang-Lee branch cut, the discontinuity of $\mathcal{M}_1(\eta)$ is a smooth function on $Y_0 < y < +\infty$, and determines the behaviour of $\mathcal{M}_1(\eta)$ on the η -plane via M_1 extended dispersion integral, which will be formulated as follows.

At generic complex η on Fig.7(b), the contour integration reproducing $\mathcal{M}_1(\eta)$ (with two terms subtracted) reads:

$$\begin{aligned} \mathcal{M}_1(\eta) - \left(M_1^{(0)} + M_1^{(1)}\eta \right) &= \eta^2 \oint_{\mathcal{C}_\eta} \frac{d\eta'}{2\pi i} \frac{\mathcal{M}_1(\eta') - M_1^{(0)} - M_1^{(1)}\eta'}{\eta'^2(\eta' - \eta)} \quad (3.4) \\ &= \eta^2 \int_{Y_0}^{+\infty} \frac{dy}{2\pi i} \left(\frac{\mathcal{M}_1(ye^{+\frac{11\pi i}{15} + i0}) - \mathcal{M}_1(ye^{+\frac{11\pi i}{15} - i0})}{y^2 e^{+\frac{11}{15}\pi i} (ye^{+\frac{11}{15}\pi i} - \eta)} + \frac{\mathcal{M}_1(ye^{-\frac{11\pi i}{15} + i0}) - \mathcal{M}_1(ye^{-\frac{11\pi i}{15} - i0})}{y^2 e^{-\frac{11}{15}\pi i} (ye^{-\frac{11}{15}\pi i} - \eta)} \right), \quad (3.5) \end{aligned}$$

where \mathcal{C}_η denotes a small contour circling counterclockwise around η . In (3.5), \mathcal{C}_η is deformed into the integration from $\eta' = e^{\frac{11\pi i}{15}} Y_0$ to $\eta' = e^{\frac{11\pi i}{15}} (+\infty)$ with its complex conjugation¹². The

¹²By $\mathcal{M}_1(\eta)$ is a real function when η is real, at complex η $\mathcal{M}_1(\eta^*) = (\mathcal{M}_1(\eta))^*$.

coefficients $M_1^{(0)}$ and $M_1^{(1)}$ in (3.4) are known exactly [17][1], and the numerical values were given in Tab.1.

Now we discuss the discontinuity on the numerator of (3.5). After rotating the branch cuts, (3.2) gives $\mathcal{M}_1(\eta)$ on the lower edge of Yang-Lee branch cut at $\eta = ye^{\pm(\frac{11}{15}\pi i + i0)}$, which sits on the high-T wedge side. On the rays $\text{Arg } \eta = \pm\frac{11}{15}\pi$, $\mathcal{M}_1(\eta = -ye^{\pm\frac{4\pi i}{15}})$ is a single-valued function for $y \leq Y_0$, and for $y > Y_0$ we denote:

$$\begin{aligned}\mathcal{M}_1(ye^{+\frac{11\pi i}{15} \pm i0}) &= e^{+\frac{11\pi i}{15}} \bar{\mathcal{M}}_1(y \pm i0), \\ \mathcal{M}_1(ye^{-\frac{11\pi i}{15} \mp i0}) &= e^{-\frac{11\pi i}{15}} \bar{\mathcal{M}}_1(y \mp i0),\end{aligned}\tag{3.6}$$

as the definition for $\bar{\mathcal{M}}_1(y \pm i0)$. Unlike in Fig.7(a), $\bar{\mathcal{M}}_1(y \pm i0)$ are not complex conjugation of each other, and the discontinuity of the extended dispersion relation is defined as:

$$\Delta_1(y) = \frac{1}{2i} \left[\bar{\mathcal{M}}_1(y + i0) - \bar{\mathcal{M}}_1(y - i0) \right],\tag{3.7}$$

which is a complex function for $y \geq Y_0$. With the help of (3.7), (3.5) is reduced as:

$$\mathcal{M}_1(\eta) = M_1^{(0)} + M_1^{(1)}\eta + \frac{2\eta^2}{\pi} \int_{Y_0}^{\infty} \frac{dy y \Re e \left(e^{-\frac{11\pi i}{15}} \Delta_1(y) \right) - \eta \Re e \Delta_1(y)}{y^2 - 2 \cos\left(\frac{11\pi}{15}\right)\eta y + \eta^2}.\tag{3.8}$$

We call (3.8) the M_1 extended dispersion relation. If the M_1 extended analyticity conjecture is correct, (3.8) should work for any complex η on Fig.7(b), including the ones in shadow domain.

Comparing to the extended dispersion relation of free energy density (see eq.(4.8) in [2]), (3.8) is simpler. The Onsager's singularity and other subtractions are absent in the M_1 extended dispersion relation (3.8). The integration (3.8) converges, because $\lim_{y \rightarrow +\infty} \Re e \Delta_1(y) = 0$, and no further subtraction is needed.

On the discontinuity $\Delta_1(y)$

With the conjecture of M_1 extended analyticity, there exist no singularity on the rotated Yang-Lee branch cut, and the discontinuity $\Delta_1(y)$ is a continuous complex function on the interval $Y_0 \leq y < +\infty$. The approximation of $\Delta_1(y)$ can be achieved by using its behaviours near $y = Y_0$ and $y = +\infty$, namely the Yang-Lee singular expansion (1.12), and the expansions at $\eta = \infty$ (equivalently $\xi = 0$, see (2.2) and (1.27)). Here we shall establish the approximation of $\Delta_1(y)$ as follows.

In the close vicinity of $y = Y_0$, $\Delta_1(y)$ is controlled by the singular expansions based on Yang-Lee criticality. Before the rotation of branch cuts (see Fig.7(a)), the function $\hat{\mathcal{M}}_1(y)$, which was defined in (3.2), is single-valued at $y > Y_0$, and admits the singular expansion:

$$\hat{\mathcal{M}}_1(y) = (y - Y_0)^{\frac{5}{12}} \left[\tilde{b}_0 + \tilde{c}_0(y - Y_0)^{\frac{5}{6}} + \tilde{b}_1(y - Y_0) + \dots \right],\tag{3.9}$$

which works in close vicinity of the Yang-Lee point $y = Y_0$. Coefficients in (3.9) read [1][5]:

$$\tilde{b}_0 = 3.0754, \quad \tilde{b}_1 = 0.8932, \quad \tilde{c}_0 = -0.9412.\tag{3.10}$$

The singular expansion (3.9) illustrates two branches of $\hat{\mathcal{M}}_1(y)$ on the both edges of Yang-Lee branch cut in Fig.7(a), which reads (with $y < Y_0$):

$$\hat{\mathcal{M}}_1(y \pm i0) = (Y_0 - y)^{\frac{5}{12}} [\tilde{b}_0 e^{\pm \frac{5\pi i}{12}} + \tilde{c}_0 (Y_0 - y)^{\frac{5}{6}} e^{\pm \frac{5\pi i}{4}} + \tilde{b}_1 (Y_0 - y) e^{\pm \frac{17\pi i}{12}} + \dots], \quad (3.11)$$

The corresponding discontinuity in Fig.7(a), before the rotation of the Yang-Lee branch cut, can be expanded as:

$$\begin{aligned} \hat{\Delta}_1(y) &= \frac{1}{2i} [\hat{\mathcal{M}}_1(y + i0) - \hat{\mathcal{M}}_1(y - i0)] \\ &= \Theta(Y_0 - y) (Y_0 - y)^{\frac{5}{12}} [\tilde{b}_0 \sin(\frac{5\pi}{12}) + \tilde{c}_0 (Y_0 - y)^{\frac{5}{6}} \sin(\frac{5\pi}{4}) + \tilde{b}_1 (Y_0 - y) \sin(\frac{17\pi}{12}) + \dots], \end{aligned} \quad (3.12)$$

which is a real function for $y < Y_0$. The rotation of Yang-Lee branch cut, as from Fig.7(a) to Fig.7(b), suggests that the singular expansion representing $\Delta_1(y)$ is a straightforward continuation of (3.12), as

$$\begin{aligned} \Delta_1(y) &= \hat{\Delta}_1(Y_0 - (y - Y_0)e^{i\pi}) \\ &\simeq \Theta(y - Y_0) (y - Y_0)^{\frac{5}{12}} \left\{ \tilde{b}_0 \sin(\frac{5\pi}{12}) e^{\frac{5\pi i}{12}} + \tilde{c}_0 \sin(\frac{5\pi}{4}) e^{\frac{5\pi i}{4}} (y - Y_0)^{\frac{5}{6}} + \tilde{b}_1 \sin(\frac{17\pi}{12}) e^{\frac{17\pi i}{12}} (y - Y_0) + \dots \right\}, \end{aligned} \quad (3.13)$$

which holds for $y > Y_0$ in a close vicinity of the Yang-Lee point. Unlike (3.12), $\Delta_1(y)$ is a complex function, with both $\Re \Delta_1(y)$ and $\Im \Delta_1(y)$ contributing to the integral (3.8).

Next we switch to the behaviour of $\Delta_1(y)$ at $y \rightarrow +\infty$. At $|\eta| \rightarrow +\infty$, from (3.1):

$$\mathcal{M}_1(\eta) \xrightarrow{|\eta| \rightarrow \infty} \begin{cases} 2\eta & |\text{Arg } \eta| < \frac{11}{15}\pi \\ -\eta & |\text{Arg } \eta| > \frac{11}{15}\pi \end{cases}, \quad (3.14)$$

which suggests $\Delta_1(y) \sim \frac{3}{2}iy$ at $y \rightarrow +\infty$. The subleading behaviours at large y follow the different expansions of \hat{M}_1 in high-T and low-T regimes at small ξ . When $T < T_c$, $\hat{M}_1(\xi)$ can be expanded in the series of $\xi^{\frac{2}{3}}$ plus corrections (see (1.27)). Differently when $T > T_c$, $\hat{M}_1(\xi^2)$ is expanded in integer powers of ξ^2 due to the unbroken \mathbb{Z}_2 symmetry. As a result, $\mathcal{M}_1(\eta)$ behaves as:

$$\mathcal{M}_1(\eta) = \eta \left(2 + \sum_{k=1}^{\infty} a_1^{(k)} \eta^{-\frac{5}{4}k} + \sum_{l=4}^{\infty} b_1^{(l)} \eta^{-\frac{5}{8}(2l+1)} \right) \quad \text{for } |\text{Arg } \eta| < \frac{11}{15}\pi, \quad (3.15)$$

$$\mathcal{M}_1(\eta) = \eta \left(-1 + \sum_{k=1}^{\infty} \mu_{2k} \eta^{-\frac{15}{4}k} \right) \quad \text{for } |\text{Arg } \eta| > \frac{11}{15}\pi, \quad (3.16)$$

at large $|\eta|$, where the coefficients in (3.15) are related to the ones in (1.27) via

$$a_1^{(k)} = (2\bar{s})^{\frac{2k}{3}} c_1^{(k)}, \quad b_1^{(l)} = (2\bar{s})^{\frac{2l+1}{3}} d_1^{(l)}. \quad (3.17)$$

Since $b_1^{(l)}$ corrections enter $\mathcal{M}_1(\eta)$ with at least $\eta^{-\frac{37}{8}}$, we will ignore them in the following analysis. Some values of leading $a_k = a_1^{(k)}$ are available in Tab.1, while various coefficients μ_{2k} were measured or computed by high-T dispersion relation (see [1]), as

$$\mu_2 \simeq 10.7620, \quad \mu_4 \simeq -97.22, \quad \mu_6 \simeq 1396. \quad (3.18)$$

Based on the expansion (3.15) and (3.16), the discontinuity $\Delta_1(y)$ at $y \rightarrow +\infty$ behaves as:

$$\Delta_1(y) = y \left(\frac{3}{2}i + \frac{i}{2} \sum_{k=1}^{\infty} a_k y^{-\frac{5}{4}k} e^{-\frac{11}{12}k\pi i} - \frac{i}{2} \sum_{k=1}^{\infty} \mu_{2k} y^{-\frac{15}{4}k} e^{-\frac{11}{4}k\pi i} \right), \quad (3.19)$$

However, (3.19) can be only understood as an asymptotic expansion, namely with zero radius of convergence. Based on the analyticity shown in Fig.1, (3.16) is convergent for $|\eta| > Y_0$ or $|\xi| < \xi_0$. However, the other expansion (3.15) can only be understood as asymptotic at complex η , due to the existence of instanton-like corrections (see Appendix B). Numerically speaking, similar to the case of low-T analysis, the instanton-like terms are negligible, and will be ignored in the following numerical analysis.

To approximate $\Delta_1(y)$ on the interval $Y_0 \leq y < +\infty$, interpolation can be used by matching both the expansions (3.19) and (3.13). The details of interpolation are presented in Appendix A. As a result of interpolation, the real and imaginary parts of discontinuities are as shown in Fig.8, where we have defined $\chi = 1/y$ and plot the function $\mathcal{E}_1(\chi) = \chi \Delta_1(y = 1/\chi)$ on the interval $0 \leq \chi \leq \mathcal{X}_0 = 1/Y_0$. The imaginary part $\Im \mathcal{E}_1(\chi)$ stays positive on the interval, with $\Im \mathcal{E}_1(\chi = 0) = \frac{3}{2}$. The real part $\Re \mathcal{E}_1(\chi)$ changes from negative to positive when χ increases from 0 to \mathcal{X}_0 . With the approximation of $\Delta_1(y)$ as in Fig.8, numerical verifications of M_1 extended dispersion relation can be achieved.

Check of M_1 extended dispersion relation

The first direct check is to compare the dispersion integral (3.8) with numerical data of $\mathcal{M}_1(\eta)$ at real η . Approximated $\Delta_1(y)$ from interpolation (see Fig.8) are used for the numerical integration in (3.8), and (3.8) is to be compared with numerical data of $\mathcal{M}_1(\eta)$ measured from the truncated spectrum on the interval $-4.0 < \eta < +4.0$. The data of $\mathcal{M}_1(\eta)$ are with 4 to 5 digits accuracy. The results of comparison are as shown in Fig.9 and Fig.10, with presenting scaling functions \mathcal{M}_1 and \hat{M}_1 (M_1 measured in unit of $|h|^{8/15}$ or $|m|$) respectively. Both Fig.9 and Fig.10 are showing agreement in good accuracy on the interval of $-4.0 \leq \eta \leq +4.0$. The evidence is supporting the conjecture of extended analyticity.

Apart from direct comparing the M_1 data with the integral (3.8), another independent verification can be made by checking expansion coefficients at small η . By expanding the integration (3.8), coefficients $M_1^{(n)}$ (see (2.1)) or (2.2) can be represented as dispersion integrations. On the other hand, some of $M_1^{(n)}$ are known and can be served as consistency checks. By using the discontinuities shown in Fig.8, these integrations read:

$$M_1^{(2)} = 0.2002 \quad \text{while} \quad -\frac{2}{\pi} \int_{Y_0}^{+\infty} \frac{dy}{y^3} \Re e \left(e^{\frac{4\pi i}{15}} \Delta_1(y) \right) \approx 0.2051, \quad (3.20)$$

$$M_1^{(3)} = -0.051 \quad \text{while} \quad +\frac{2}{\pi} \int_{Y_0}^{+\infty} \frac{dy}{y^4} \Re e \left(e^{\frac{8\pi i}{15}} \Delta_1(y) \right) \approx -0.050, \quad (3.21)$$

$$M_1^{(4)} \text{ is unknown,} \quad \text{while} \quad +\frac{2}{\pi} \int_{Y_0}^{+\infty} \frac{dy}{y^5} \Re e \left(e^{-\frac{\pi i}{5}} \Delta_1(y) \right) \approx -0.0083, \quad (3.22)$$

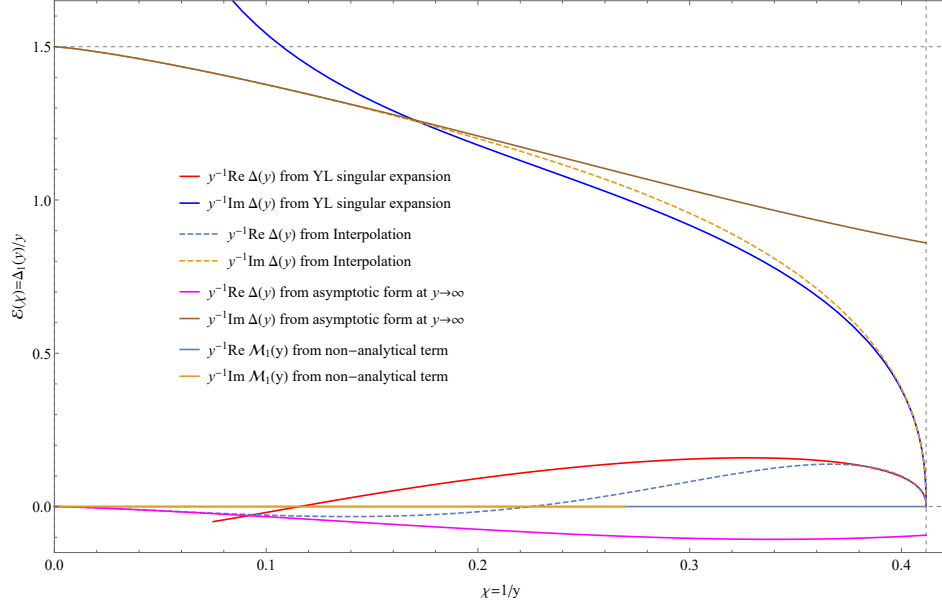


Figure 8. The plot illustrating the real and imaginary parts of function $\mathcal{E}_1(\chi) = \chi \Delta_1(y = 1/\chi)$. The horizontal axis is $\chi = 1/y$ on the interval $[0, \mathcal{X}_0]$, with the Yang-Lee point is located at $\mathcal{X}_0 = 1/Y_0$. Singular expansion (3.13) was plotted in red and blue solid lines, as real and imaginary parts. The expansion (3.19) at $y = \infty$ or $\chi = 0$ was plotted in magenta and brown solid lines. The dashed curves are the interpolations of $\mathcal{E}_1(\chi)$ between (3.13) and (3.19), see (A.6) and (A.8) in Appendix A. The dashed curves serve as good approximations for the real and imaginary part of $\Delta_1(y)$ along the rotated Yang-Lee branch cut. Finally, the two solid lines which almost overlapping with horizontal axis represents the contribution of instanton-like terms. They are as continuing $z \rightarrow ye^{\frac{\pi}{5}}$ in (B.35), see Appendix B for more details. Their contribution to the dispersion integral (3.8) is negligible.

where $M_1^{(2)}$ was given in Tab.1, $M_1^{(3)}$ was also measured in [1], and there's no known numerical value of $M_1^{(4)}$ available. The above comparison of $M_1^{(2)}$ and $M_1^{(3)}$ are showing good agreement, with deviations less than 3%.

Furthermore, we should check (3.8) not only at real η but also works when η is complex. The verification can be made by computing (3.8) for $\mathcal{M}_1(\eta)$ at $\eta = -ye^{\pm \frac{4}{15}\pi i}$ with $0 < y < Y_0$. On this interval between the Yang-Lee point and the E_8 point, the function $\mathcal{M}_1(\eta = -ye^{\mp \frac{4\pi i}{15}})$ is complex, and can be related to the values of $\hat{M}_1(\xi^2)$ on the upper/lower edges of the Yang-Lee branch cut, as (3.3). Unfortunately, the measurement of $\hat{M}_1(\xi^2 \pm i0)$ for $\xi^2 < -\xi_0^2$ are with poor accuracy (see discussions and Fig.18 in [1]), thus we shall verify complex (3.8) by comparing it to the expansions at $\eta = 0$ and $\eta = -Y_0e^{\pm \frac{4}{15}\pi i}$ instead, with both real and imaginary parts. Near the Yang-Lee point the numerical integration is to be compared with:

$$\bar{\mathcal{M}}_1(y) = (Y_0 - y)^{\frac{5}{12}} \left[\tilde{b}_0 e^{+\frac{5\pi i}{12}} + \tilde{c}_0 (Y_0 - y)^{\frac{5}{6}} e^{+\frac{5\pi i}{4}} + \tilde{b}_1 (Y_0 - y) e^{+\frac{17\pi i}{12}} + \dots \right]. \quad (3.23)$$

based on (3.9), and near $y = 0$ the E_8 point the numerical integration is be compared with (1.13) with complex $\eta = ye^{\pm \frac{11\pi i}{15}}$. The results are as shown in Fig.11, with good accordance on the interval $0 \leq y \leq Y_0$ for both real and imaginary part.

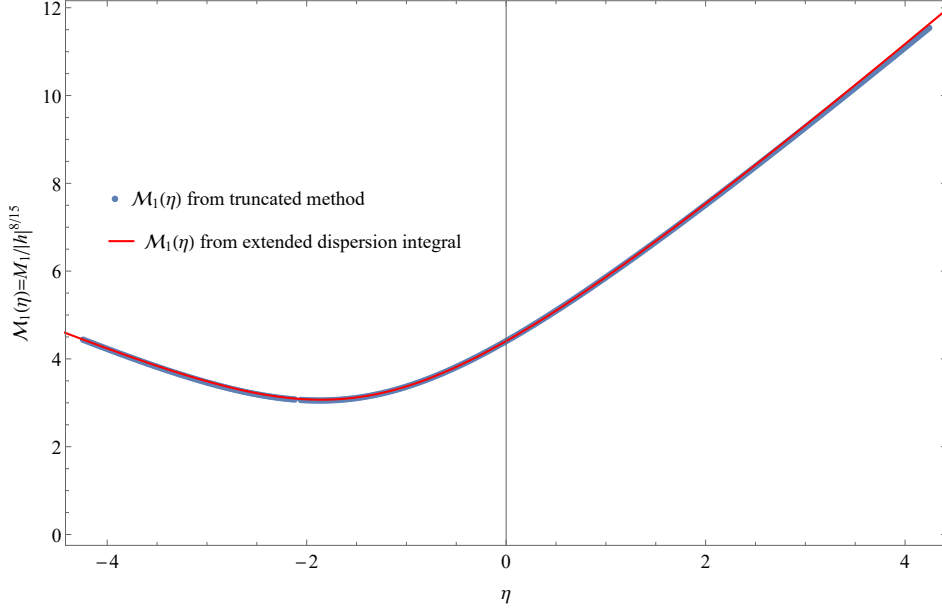


Figure 9. A direct verification of M_1 extended dispersion relation, by comparing the function $\mathcal{M}_1(\eta)$ via dispersion relation (3.8) and the truncated data (see Fig.3). Numerical data of $\mathcal{M}_1(\eta)$ are as shown in bullets, which were measured using TFFSA with 5 to 6 digits accuracy. The dispersion integral (3.8) is given by red solid curve, with using $\Delta_1(y)$ approximated by the interpolation in Appendix A, see (A.6), (A.8) and Fig.8.

In summary, the verifications of M_1 extended dispersion relation are given at real η , as comparing the truncated data of $\mathcal{M}_1(\eta)$ to the numerical integration (3.8), see Fig.9 and Fig.10). These results, combined with two other cross checks, as comparing the expansion coefficients $M_1^{(k)}$ (see (3.20), (3.21) & (3.22)), and as comparing (3.8) with complex η to the expansions (3.9) and (1.13) (see Fig.11). All this evidence strongly support the extended analyticity conjecture of M_1 , as illustrated in Fig.7(b), that no other singularity exist within the shadowed domain or along the rotated Yang-Lee branch cut.

4 Summary and discussion

In this work, we continue the study on IFT spectrum of the first mass M_1 (see [1]). Analyticity of M_1 was conjectured in the low-T regime, as in Fig.2 and (2.10). Numerical approximation of the discontinuities along the Fisher-Langer's branch cut was established (see Fig.5), and with its help, the low-T analyticity was verified from various aspects, as in Fig.2.14, and (2.14). Furthermore, on the complex η -plane the extended analyticity conjecture of M_1 was formulated, which unifies the behaviours of M_1 in both high-T and low-T regimes. The complex structure of $\mathcal{M}_1(\eta)$ on the complex η plane is as shown in Fig.7(b), with the rotation of Yang-Lee branch cut. The associated extended dispersion relation of M_1 was given in (3.8), which depends on the discontinuities $\Delta_1(y)$ along the rotated Yang-Lee branch cut.

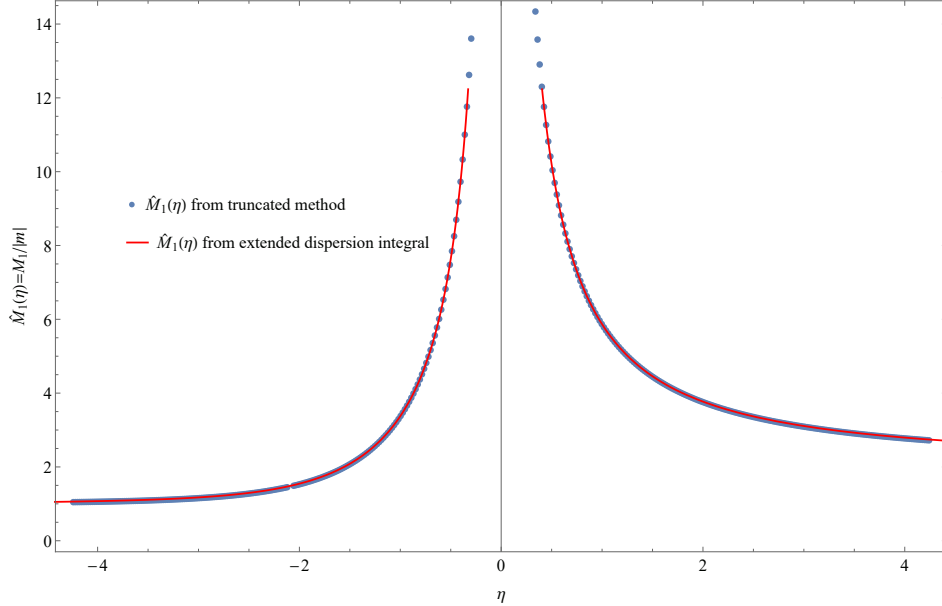


Figure 10. Similar to Fig.9, a direct comparison of function $\hat{M}_1 = \mathcal{M}_1(\eta)/|\eta|$ between the dispersion integral of (3.8) and the numerical data. The vertical axis is now \hat{M}_1 , as mass of the lightest particle measured in unit of $|m|$. Numerical data from TFFSA are in bullets, and the dispersion integration (3.8) is represented in red solid curve, using discontinuities from the interpolation of Appendix A. The horizontal axis is η , which is related to ξ via $\eta = -\xi^{-\frac{8}{15}}$ in the high-T regime, and $\eta = \xi^{-\frac{8}{15}}$ in the low-T regime.

The approximation of $\Delta_1(y)$, based on the expansions (3.13) and (3.19), are presented in Fig.8, with the details given in Appendix A. With its help, the extended dispersion relation (3.8) were verified with various comparisons, as with the truncated data (Fig.9 & Fig.10), of the η -expansion coefficients ((3.20) & (3.21)), and at complex η to the expansions (3.23) & (1.13) (see Fig.11). All of which show good accordance (deviations $< 3\%$), and support the conjecture of M_1 extended analyticity conjecture.

Our extended analyticity conjecture of M_1 is in agreement with the one of the free energy density, which was conjectured and verified in [2]. Both extended analyticity conjectures state that no other singularity exist within the shadowed domain (domain of $\frac{8}{15}\pi < |\text{Arg } \eta| < \frac{11}{15}\pi$, see Fig.7(b)). However, there are several major differences between the M_1 extended dispersion relation (3.8) and the dispersion relation of free energy density (see (4.8) of [2]). Firstly, the order of divergences at $|\eta| \rightarrow \infty$ and subtractions are different. $\mathcal{M}_1(\eta)$ is divergence with $O(\eta)$ at $|\eta| \rightarrow \infty$, thus the subtractions are of $M_1^{(0)} + M_1^{(1)}\eta$. Meanwhile, function $\tilde{\Phi}(\eta)$ (the scaling function of free energy density, defined in (3.20) & (3.25) of [2]) has more complicated behaviours at $|\eta| \rightarrow \infty$, as a combination of Onsager's singularity $\sim \eta^2 \log \eta^2$ and series expansion in fractional powers of η (see (3.35) & (3.36) of [2]). As a result, the extended dispersion relation of free energy density is much more complicated comparing to (3.8). Secondly, the discontinuities along the rotated Yang-Lee branch cut have very different

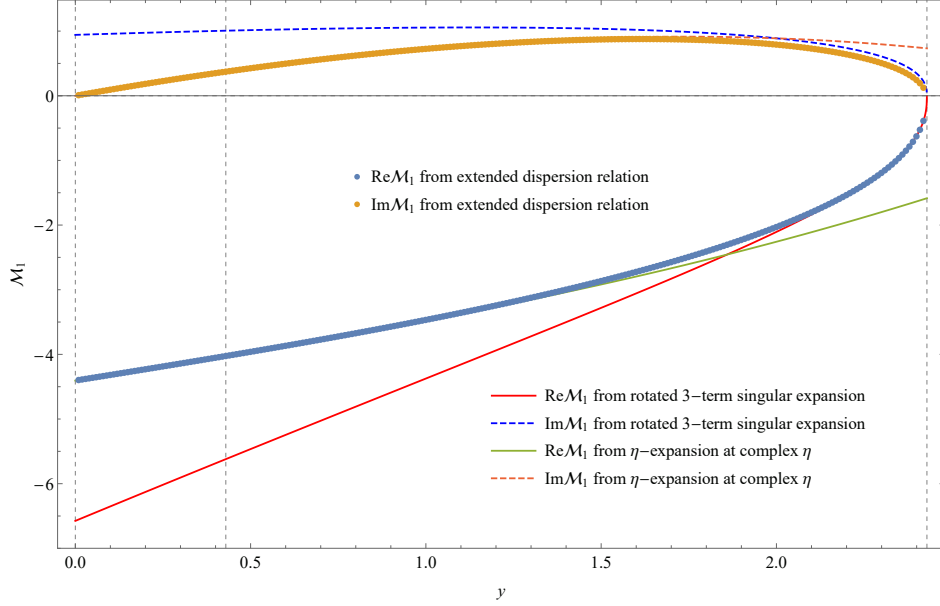


Figure 11. A verification of M_1 extended dispersion relation at complex $\eta = ye^{\frac{11}{15}\pi i}$. Dispersion integral (3.8) is plotted for $\eta = ye^{\frac{11}{15}\pi i}$ and $0 < y < Y_0$, with real and imaginary parts as bullets in different colors. They are to be compared to the series expansions at $y = Y_0$ and $y = 0$. Near the Yang-Lee point, the real and imaginary parts of (3.23) are plotted as red solid curve and blue dashed curve. Near $y = 0$, (1.13) is plotted with $\eta \rightarrow ye^{\pm \frac{11}{15}\pi i}$, with the truncation till the term with $M_1^{(3)}$. The real and imaginary part are plotted as green solid curve and pink dashed curve. The dispersion integral (3.8) matches well with (3.23) near $y = Y_0$, and with (1.13) near $y = 0$.

behaviours. According to the analysis in Sec.3 and Appendix B, the contributions to $\Delta_1(y)$ at $y \rightarrow +\infty$ are mostly controlled by the expansions of \hat{M}_1 at small ξ , with the instanton-like contribution negligible. However, the discontinuity of $\tilde{\Phi}(\eta)$ is significantly contributed by the instanton-like terms ($\sim y^{1/8} \exp(-\frac{\pi}{28}e^{-\frac{3\pi i}{8}}y^{15/8})$, see (8.19) of [2]). The reason was explained in the introduction between (1.17) and (1.18), as since (1.17) has vanishing continuation along the Fisher-Langer's branch cut, the discontinuity of free energy density is determined by the instanton-like term (1.18), and same as it continued across the shadowed domain.

In Sec.2, we also analyzed the analyticity of functions $\hat{M}_2(\xi)$ and $\hat{M}_3(\xi)$ in the low-T ξ -plane, which are as shown in Fig.2. However, for the second mass M_2 and third mass M_3 , the analyticities of their corresponding scaling functions $\mathcal{M}_2(\eta)$ and $\mathcal{M}_3(\eta)$ on the complex η plane, if exist, should be more involved, comparing to the M_1 extended analyticity conjecture and the dispersion relation (3.8). The reason is that in the high-T regime $T > T_c$, at finite ξ_2 and ξ_3 , the masses of second particle and third particle exceed $2M_1$, and the particles become unstable. For $\xi^2 < \xi_2^2$ or $\xi^2 < \xi_3^2$, the scaling functions $\hat{M}_2(\xi^2)$ and $\hat{M}_3(\xi^2)$ are neither measurable via truncated method nor have good analyticity properties. Furthermore, little is known about what the Yang-Lee singularities means for the higher particles, not to mention the behaviours of discontinuities of associated scaling functions (if not using \hat{M}_p or

\mathcal{M}_p) along the Yang-Lee branch cut. Still, there exist evidences of a continuous evolution of the Ising mass spectrum along the real η axis [3], which suggest the possibility of higher masses extended analyticities with much more involved forms. We hope to return to this topic in the future.

Acknowledgments

The author is most thankful to A. B. Zamolodchikov for illuminating discussions and advices on the manuscript. I also thank P. Vieira, R. Shrock and B. McCoy for helpful discussions. Research of HLX is partly supported by NSF under grant PHY-2210533.

Appendix

A Numerical approximation of $\Delta_1(y)$ from interpolation

In this section, we will provide details of the interpolation which gives the numerical approximation of $\Re \mathcal{E}_1(y)$ and $\Im \mathcal{E}_1(y)$, as shown in Fig.8. The interpolation method is similar to what were discussed in [2],[1] and[4].

Following (3.19) and using parameter $\chi = 1/y$, $\mathcal{E}_1(\chi) = \chi \Delta_1(y = \frac{1}{\chi})$ admits the asymptotic expansion at $\chi = 0$, as:

$$\mathcal{E}_1(\chi) = \frac{3}{2}i + \frac{i}{2} \sum_{k=1}^{\infty} a_k \chi^{\frac{5}{4}k} e^{-\frac{11}{12}k\pi i} - \frac{i}{2} \sum_{k=1}^{\infty} \mu_{2k} \chi^{\frac{15}{4}k} e^{-\frac{11}{4}k\pi i}. \quad (\text{A.1})$$

Define $t = \chi^{\frac{5}{4}}$, (A.1) becomes:

$$\Im \mathcal{E}_1 = \frac{3}{2} + \frac{1}{2} \sum_{k=1}^{\infty} a_k t^k \cos\left(\frac{11\pi k}{12}\right) - \frac{1}{2} \sum_{l=1}^{\infty} \mu_{2l} t^{3l} \cos\left(\frac{11\pi l}{4}\right), \quad (\text{A.2})$$

$$\Re \mathcal{E}_1 = \frac{1}{2} \sum_{k=1}^{\infty} a_k t^k \sin\left(\frac{11\pi k}{12}\right) - \frac{1}{2} \sum_{l=1}^{\infty} \mu_{2l} t^{3l} \sin\left(\frac{11\pi l}{4}\right), \quad (\text{A.3})$$

which works near $t = 0$. On the other hand, near the Yang-Lee point $y = Y_0$ or equivalently $t = T_0 := Y_0^{-\frac{5}{4}}$, \mathcal{E}_1 admits singular expansion in powers of $(T_0 - t)$:

$$\begin{aligned} \mathcal{E}_1 = (T_0 - t)^{\frac{5}{12}} \left\{ \hat{b}_0 \sin\left(\frac{5\pi}{12}\right) e^{\frac{5\pi i}{12}} + \hat{c}_0 \sin\left(\frac{5\pi}{4}\right) e^{\frac{5\pi i}{4}} (T_0 - t)^{\frac{5}{6}} \right. \\ \left. + \hat{b}_1 \sin\left(\frac{17\pi}{12}\right) e^{\frac{17\pi i}{12}} (T_0 - t) + \dots \right\}, \end{aligned} \quad (\text{A.4})$$

which follows (3.13), with the coefficients \hat{b}_0 , \hat{b}_1 and \hat{c}_0 were computed from (3.10), as:

$$\hat{b}_0 = 2.6511, \quad \hat{b}_1 = -1.121, \quad \hat{c}_0 = -3.558. \quad (\text{A.5})$$

(A.4) can be further extended with more terms, and the exponents of the additional terms follow the operator contents of Yang-Lee CFT and dimensional analysis [1][4]. In addition to (A.4), we add 4 more terms as:

$$\begin{aligned} \mathcal{E}_1^{\text{Approx}} = & \text{(A.4)} + \hat{e}_0 \sin\left(\frac{25\pi}{12}\right) e^{\frac{25\pi i}{12}} (T_0 - t)^{\frac{25}{12}} + \hat{c}_1 \sin\left(\frac{9\pi}{4}\right) e^{\frac{9\pi i}{4}} (T_0 - t)^{\frac{9}{4}} \\ & + \hat{b}_2 \sin\left(\frac{29\pi}{12}\right) e^{\frac{29\pi i}{12}} (T_0 - t)^{\frac{29}{12}} + \hat{d}_0 \sin\left(\frac{11\pi}{4}\right) e^{\frac{11\pi i}{4}} (T_0 - t)^{\frac{11}{4}}, \end{aligned} \quad (\text{A.6})$$

with \hat{e}_0 , \hat{c}_1 , \hat{b}_2 and \hat{d}_0 are four unknown coefficients. These coefficients are determined by requiring 4 constraints as:

$$\mathcal{E}_1^{\text{Approx}} \Big|_{t=0} = \mathcal{E}_1 \Big|_{t=0}, \quad \text{and} \quad \frac{d}{dt} \mathcal{E}_1^{\text{Approx}} \Big|_{t=0} = \frac{d}{dt} \mathcal{E}_1 \Big|_{t=0}, \quad (\text{A.7})$$

for real and imaginary parts individually. The right hand sides follow the expansions (A.2) and (A.3) at $t = 0$, with:

$$\begin{aligned} \Re \mathcal{E}_1 \Big|_{t=0} &= 0, & \frac{d}{dt} \Re \mathcal{E}_1 \Big|_{t=0} &= -0.5844, \\ \Im \mathcal{E}_1 \Big|_{t=0} &= 1.5, & \frac{d}{dt} \Im \mathcal{E}_1 \Big|_{t=0} &= -2.181, \end{aligned}$$

the numerical solution of extra coefficients are:

$$\hat{e}_0 = -24.69, \quad \hat{c}_1 = -15.83, \quad \hat{b}_2 = 27.38, \quad \hat{d}_0 = -32.30. \quad (\text{A.8})$$

As a result, we take the 7-term expansion (A.6), where the coefficients are (A.5) & (A.8), with the parameter t transformed back to $\chi = t^{4/5} = 1/y$, as the numerical approximations of $\mathcal{E}_1(\chi)$ along the rotated Yang-Lee branch cuts. Real and imaginary parts of the approximation $\mathcal{E}_1^{\text{Approx}}(\chi)$ were the ones as shown in Fig.8, and reproduce the numerical verification of M_1 extended dispersion relation as was discussed in Sec.3.

B Computing the non-analytic term \mathcal{K}_p .

In this section, we shall analyze the "instanton-like" contribution of M_1 in the low-T regime and its continuation. The analysis follows the theory of condensation of nucleation, see [20–26] for more detailed discussions.

As was discussed in the introduction, when $T < T_c$ and exist a small nonvanishing external magnetic field h , the double degenerate vacua (1.15) are shifted, splitted into the stable vacuum (spins align along the external field) and metastable vacuum (spins align against the external field). The continuation $h \rightarrow e^{\pm\pi i} h$ can be interpreted as flipping the direction of external magnetic field, thus the roles of stable and metastable vacua are interchanged. As a result, thermodynamic quantities at $\xi \rightarrow 0^-$ should be understood as of those in the metastable phase. For example, $M_1(m, -h \pm i0)$ should be understood as the inverse correlation length in the metastable phase, and is contributed by both the term-by-term continuation the term-by-term

continuation (2.6) and the instanton-like term. Here we denote the term-by-term contribution of $M_1(m, -h \pm i0)$ as $\tilde{M}_1^{(\pm)} = \tilde{M}_1^{(\pm)}(m, \mathfrak{h}) = M_1(m, e^{\pm\pi i} \mathfrak{h})$, where \mathfrak{h} is the external field¹³, and the instanton-like term $K_1(m, \mathfrak{h})$ is defined as:

$$M_1(m, -h \pm i0) = \tilde{M}_1^{(\pm)}(m, \mathfrak{h}) \pm K_1(m, \mathfrak{h}). \quad (\text{B.1})$$

The dimensionless scaling function of K_1 is defined by:

$$\mathcal{K}_1(\tilde{\lambda}) = \frac{1}{m} K_1(m, \mathfrak{h}), \quad \text{where} \quad \tilde{\lambda} = \frac{2\bar{\sigma}\mathfrak{h}}{m^2} = 2\bar{s}x > 0, \quad (\text{B.2})$$

and $x = \mathfrak{h}/m^{15/8} = -\xi > 0$.

At finite temperature, the metastable vacuum is perturbed by thermal fluctuations. Microscopically, thermal fluctuations generate clusters of spins align along the external field, with satisfying certain distributions. Among them, sufficiently large clusters would stabilize their shapes as round circles, and can be interpreted as bubbles of stable vacuum. Assume the bubbles are circular with radius R , the one bubble effective action reads [26]:

$$\mathcal{A}_0 = +2\pi mR - 2\pi\bar{\sigma}\mathfrak{h}R^2 = +\pi mR_c - 2\pi\bar{\sigma}\mathfrak{h}(R - R_c)^2, \quad (\text{B.3})$$

which is contributed by the area term (due to the surface tension) and volume term (due to the overall energy density difference between the vacua). Here the critical radius is defined as

$$R_c = \frac{m}{2\bar{\sigma}\mathfrak{h}} = \frac{1}{m\tilde{\lambda}} = \frac{1}{2\bar{s}x \cdot m}, \quad (\text{B.4})$$

which is the saddle point of (B.3). For later convenience, (B.3) can be written in dimensionless form, with $r = mR$:

$$\mathcal{A}_0 = +\frac{\pi}{\tilde{\lambda}} - \pi\tilde{\lambda}\left(r - \frac{1}{\tilde{\lambda}}\right)^2. \quad (\text{B.5})$$

However, with the negative quadratic term of (B.3), any bubble with size $R > R_c$ would explode instantly due to instability, and lead to the decay of metastable vacuum. Such process is known as nucleation, and provides the physical interpretation of (1.18) as the metastable vacuum decay rate. The instability nature of metastable vacuum suggests that computations regarding instanton-like terms are only defined in terms of analytical continuation, and further subtleties will be discussed in this section.

In fact, the effective action (B.3) is only a rough description, because it ignores the thickness of bubble shell and the variations of bubble shape. The thickness of bubble shell can be interpreted as the size of instantons, which tunnel between the vacuums, and when $\tilde{\lambda}$ is small, or to say $2\bar{\sigma}\mathfrak{h} \ll m^2$, the tunneling size is negligible. Analysis of the latter one requires path-integration over all possible bubble shapes [26], which is as follows.

¹³On the upper/lower edge of Fisher-Langer's branch, $h = e^{\pm\pi i} \mathfrak{h}$ with $\mathfrak{h} > 0$.

To include the fluctuations of bubble shape, angular dependence is added to the radius, as using the polar coordinate (\mathcal{R}, α) ¹⁴. The one bubble effective action (B.3) becomes:

$$\mathcal{A}[\mathcal{R}] = m \int_0^{2\pi} \sqrt{\dot{\mathcal{R}}^2 + \mathcal{R}^2} d\alpha - 2\bar{\sigma}\mathfrak{h} \int_0^{2\pi} \frac{1}{2} \mathcal{R}^2 d\alpha, \quad (\text{B.6})$$

where we are replacing $R \rightarrow \mathcal{R} = \mathcal{R}(\alpha)$ and abbreviating $\dot{\mathcal{R}} = \frac{d}{d\alpha} \mathcal{R}(\alpha)$. The radius coordinate \mathcal{R} can be decomposed near the stationary configuration, as $\mathcal{R}(\alpha) = R_c + \rho(\alpha)$, where $\rho(\alpha)$ represents small deviation from R_c .

To analyze the effect of bubbles on M_1 , we consider the 2-point correlation function in metastable vacuum, which is defined as:

$$G(L) = \langle \sigma(L)\sigma(0) \rangle = \frac{\int \mathcal{D}\sigma e^{-\mathcal{A}} \sigma(L)\sigma(0)}{\int \mathcal{D}\sigma e^{-\mathcal{A}}}, \quad (\text{B.7})$$

where all possible $\sigma(x)$ configurations have been path-integrated. In the metastable vacuum, the path integrals of (B.7) can be expanded as summation over clusters of spins align along to the external field, equivalent to the bubbles of (B.6). With shorthand notation, we denote the denominator of (B.7) as:

$$\mathcal{N} = \int \mathcal{D}\sigma e^{-\mathcal{A}} = \sum_{n=0}^{\infty} \mathcal{N}_n = \mathcal{N}_0 + \sum_{n=1}^{\infty} \frac{1}{n!} \prod_{k=1}^n \left(\int_{-\infty}^{+\infty} dx_k dy_k \int_{\gamma_k} \mathcal{D}\mathcal{R}_k \right) e^{-\sum_k \mathcal{A}[\mathcal{R}_k]}, \quad (\text{B.8})$$

$$\mathcal{N}_n = \frac{1}{n!} \left(\int_{-\infty}^{+\infty} dx dy \int_{\alpha=0}^{\alpha=2\pi} \mathcal{D}\rho(\alpha) e^{-\mathcal{A}[\mathcal{R}]} \right)^n, \quad (\text{B.9})$$

where in (B.8) we have expanded \mathcal{N} by the number of bubbles, and for each bubble its coordinate (x_k, y_k) integrated. The simple closed curve γ_k is to describe the shape of bubble with labelling k , and in (B.9) the integration over bubble configurations $\int \mathcal{D}\mathcal{R}$ is replaced by $\int \mathcal{D}\rho$. Same as $\mathcal{R}(\alpha)$, function $\rho(\alpha)$ is also single-valued and periodic, with $\rho(0) = \rho(2\pi)$. Similarly, expanding the numerator of (B.7) gives:

$$\mathcal{G}(L) = \int \mathcal{D}\sigma e^{-\mathcal{A}} \sigma(L)\sigma(0) = \mathcal{G}_0(L) + \sum_{n=1}^{\infty} \mathcal{G}_n(L), \quad (\text{B.10})$$

$$\mathcal{G}_n(L) = \frac{1}{n!} \prod_{k=1}^n \left(\int_{-\infty}^{+\infty} dx_k dy_k \int_{\alpha=0}^{\alpha=2\pi} \mathcal{D}\rho_k(\alpha) \right) e^{-\sum_k \mathcal{A}[\mathcal{R}_k]} \sigma(L)\sigma(0). \quad (\text{B.11})$$

Obviously $\mathcal{G}(L)$ and each $\mathcal{G}_n(L)$ are only functions depending on L , and \mathcal{G}_0 should proportional to the spacetime volume $\text{Vol}(\mathbb{R}^2)$.

Based on (B.9) and (B.11), the 2-point correlator of the metastable phase (B.7) can be rearranged by the number of bubbles, as:

$$\langle \sigma(L)\sigma(0) \rangle = \frac{\mathcal{G}_0}{\mathcal{N}_0} + \frac{\mathcal{G}_1 - \frac{\mathcal{N}_1}{\mathcal{N}_0} \mathcal{G}_0}{\mathcal{N}_0} + \frac{\mathcal{G}_2 - \left(\frac{\mathcal{N}_2}{\mathcal{N}_0} - \frac{\mathcal{N}_1^2}{\mathcal{N}_0^2}\right) \mathcal{G}_0 - \frac{\mathcal{N}_1}{\mathcal{N}_0} \mathcal{G}_1}{\mathcal{N}_0} + \dots \quad (\text{B.12})$$

$$= G^{(0)}(L) + G^{(1)}(L) + G^{(2)}(L) + \dots, \quad (\text{B.13})$$

¹⁴In [26], it was argued that at leading order $\mathcal{R}(\alpha)$ is a single-valued function of α . The extremely concave bubble gives higher order singularity. For example, dumbbell-like bubble contributes terms $\sim e^{-\pi/\lambda^3}$.

Bubble of stable vacuum

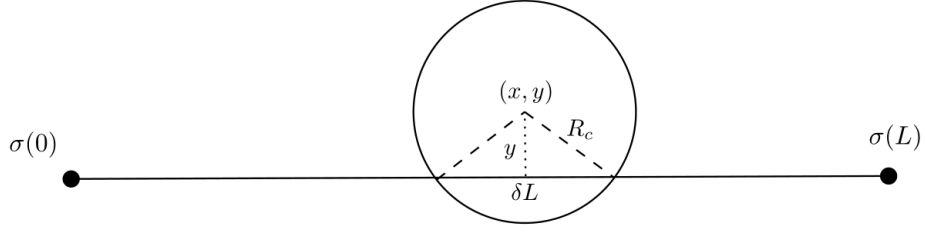


Figure 12. The contribution of one critical bubble to $\mathcal{G}_1(L)$ in (B.14). The two spin operator are inserted at $(0, 0)$ and $(L, 0)$, and the center of critical bubble is located at (x, y) . The path of particle propagating within the bubble is with length $\delta L = 2\sqrt{R_c^2 - y^2}$

with $G^{(k)}(L)$ represents the normalized k -bubble contribution. The leading term $G^{(0)} = \mathcal{G}_0/\mathcal{N}_0$ is finite, as both \mathcal{G}_0 and \mathcal{N}_0 are with divergences proportional to $\text{Vol}(\mathbb{R}^2)$. $G^{(1)}(L)$ represents the one bubble correction, with both \mathcal{G}_1 and \mathcal{N}_1 diverge with $(\text{Vol}(\mathbb{R}^2))^2$, due to the extra integral over the position of bubble. However $G^{(1)}(L)$ remains finite, by the cancellation of divergences between the two terms of its numerator.

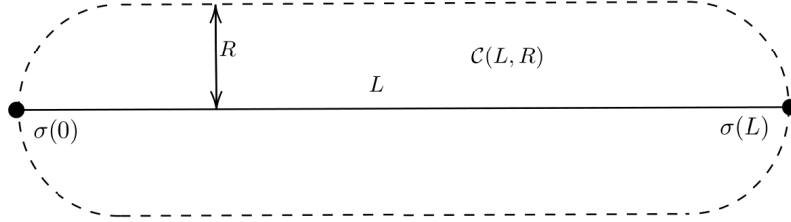


Figure 13. The cigar-like integration domain $\mathcal{C}(L, R)$ in (B.15).

To compute $G^{(1)}(L)$, consider the one bubble configuration shown as in Fig.12¹⁵. The bubble is perturbed near its critical radius, with $\mathcal{R} = R_c + \rho$, and we denoted the center of the bubble as (x, y) . In Fig.12, the path propagating within the stable vacuum bubble is with length δL , and the one bubble contribution reads:

$$G^{(1)}(L) = \frac{1}{\mathcal{N}_0} \left(\mathcal{G}_1(L) - \frac{\mathcal{N}_1}{\mathcal{N}_0} \mathcal{G}_0(L) \right) \quad (\text{B.14})$$

$$= \frac{1}{\text{Vol}(\mathbb{R}^2)} \int_{\mathcal{C}(L, R)} dx dy \int \mathcal{D}\rho(\alpha) e^{-\mathcal{A}(\mathcal{R})} \cdot \frac{e^{-\tilde{M}_1 L}}{L^{1/2}} \left(e^{(\tilde{M}_1 - M_1)\delta L} - 1 \right), \quad (\text{B.15})$$

¹⁵In the low-T regime, the lightest particle is the first meson of the McCoy-Wu scenario. The size of first meson can be understood as the maximum separation between the semiclassical trajectories of quarks, which is $X_1 = 2R_c(\cosh \vartheta_1(\lambda) - 1)$. At small λ , $X_1 \propto 1/\lambda^{1/3}$. The size of meson is much smaller than the size of critical bubble, as $X_1 \ll R_c$. As a result, in Fig.12 the size of propagating particle is negligible.

where the factor $e^{(\tilde{M}_1 - M_1)\delta L}$ is the result of the particle propagating within the bubble¹⁶, and the -1 term in (B.15) follows the second term $-\frac{N_1}{N_0^2}\mathcal{G}_0(L)$ of (B.14). The integration regime of $\int dx dy$ is the cigar-like domain $\mathcal{C}(L, R_c)$ as shown in Fig.13. When the center of bubble lies outside of the cigar, as $(x, y) \notin \mathcal{C}(L, R_c)$, two terms in (B.14) cancel with each other. When $L \gg R_c$, the cigar can be approximated as a rectangular, and (B.15) becomes:

$$G^{(1)}(L) = \frac{1}{\text{Vol}(\mathbb{R}^2)} \int_0^L dx \int_{-R_c}^{+R_c} dy \int \mathcal{D}\rho e^{-\mathcal{A}[\mathcal{R}]} \frac{e^{-\tilde{M}_1 L}}{L^{1/2}} \left(e^{(\tilde{M}_1 - M_1)\delta} - 1 \right), \quad (\text{B.16})$$

with $\delta = \delta(y, R_c) = 2\sqrt{R_c^2 - y^2}$.

(B.16) has dealt with the one bubble contribution, and if ignoring interactions between the bubbles, the multi-bubble contribution can be treated with similar manner, with the summation of (B.13) exponentiates. As a result, (B.16) is related to the instanton-like term \mathcal{K}_1 (defined in (B.2)) by (on the upper edge):

$$G^{(1)}(L) = -(mL) \frac{e^{-\tilde{M}_1 L}}{\sqrt{L}} \cdot \mathcal{K}_1(\lambda). \quad (\text{B.17})$$

and we will compute $\mathcal{K}_1(\lambda)$ by doing appropriate regularization of (B.16).

Back to (B.16), the integration of $dx dy$ over the rectangle becomes:

$$\int_0^L dx \int_{-R_c}^{+R_c} dy \left(e^{N_1 \sqrt{R_c^2 - y^2}} - 1 \right) = \pi L R_c \left(I_1(N_1 R_c) + L_{-1}(N_1 R_c) - \frac{2}{\pi} \right), \quad (\text{B.18})$$

where $N_1 = N_1(m, \mathfrak{h}) = 2\tilde{M}_1 - 2M_1$, and $I_1(z)$ & $L_{-1}(z)$ are the Bessel-I function and Struve-L function. (B.16) then becomes a path integration over $\mathcal{D}\rho$, namely the variations of the bubble shape, as:

$$G^{(1)}(L) = \frac{\pi L}{\text{Vol}(\mathbb{R}^2)} \frac{e^{-\tilde{M}_1 L}}{L^{1/2}} \int \mathcal{D}\rho e^{-\mathcal{A}[\mathcal{R}]} R_c \left(I_1(N_1 R) + L_{-1}(N_1 R) - \frac{2}{\pi} \right), \quad (\text{B.19})$$

and similar to the computation regarding free energy in [21][26], the integral $\mathcal{D}\rho$ in (B.19) counts the partition sums in metastable vacuum. In fact, (B.19) is a gaussian-like path integration, because the action $\mathcal{A}[\mathcal{R}]$ can be reduced to the action of compact boson. Expanding (B.6) near the stationary radius $\mathcal{R}(\alpha) = R_c + \rho(\alpha)$:

$$\mathcal{A}[R_c + \rho] = \mathcal{A}_0(R_c) + \frac{m}{R_c} \int_0^{2\pi} d\alpha \cdot \frac{1}{2} (\dot{\rho}^2 - \rho^2) + O(\rho^3) = \frac{\pi}{\lambda} + \mathcal{S}[\rho; R_c] + O(\varrho^3), \quad (\text{B.20})$$

$$\mathcal{S}[\rho; R_c] = \frac{m}{R_c} \int_0^{2\pi} \frac{1}{2} (\dot{\rho}^2 - \rho^2) d\alpha, \quad (\text{B.21})$$

then (B.19) becomes

$$G^{(1)}(L) = \frac{\pi L e^{-\tilde{M}_1 L}}{\sqrt{L} \text{Vol}(\mathbb{R}^2)} e^{-\frac{\pi}{\lambda}} R_c \left(I_1(N_1 R_c) + L_{-1}(N_1 R_c) - \frac{2}{\pi} \right) \int \mathcal{D}\rho e^{-\mathcal{S}}. \quad (\text{B.22})$$

¹⁶The superscript sign (\pm) of \tilde{M}_1 representing upper/lower edge is suppressed here.

When the coefficient of quadratic term ρ^2 takes the value $\omega^2 = -1$, the action \mathcal{S} of (B.21) has two extra zero modes, as:

$$\rho(\alpha) \rightarrow \rho(\alpha) + a_x \cos \alpha + a_y \sin \alpha, \quad (\text{B.23})$$

which correspond to translations in two dimensions, and gives a divergence of $\mathcal{D}\rho$ proportional to $\text{Vol}(\mathbb{R}^2)$. This divergence cancels the divergent denominator in (B.22).

With the quadratic action (B.21), the functional integration $\mathcal{D}\rho$ reproduces a partition function of a periodic boson¹⁷, and regularization of divergency gives¹⁸:

$$\int \mathcal{D}\rho e^{-\mathcal{S}[\rho;R]} = \frac{i}{2} \frac{m}{\pi R_c} \cdot \text{Vol}(\mathbb{R}^2) + (\text{finite terms}). \quad (\text{B.24})$$

Combined with (B.24), (B.22) becomes:

$$G^{(1)}(L) = \frac{e^{-\tilde{M}_1 L}}{\sqrt{L}} mL \cdot \frac{i}{2} \left(I_1(N_1 R_c) + L_{-1}(N_1 R_c) - \frac{2}{\pi} \right) e^{-\frac{\pi}{\tilde{\lambda}}}, \quad (\text{B.25})$$

and from (B.17), the instanton-like term reads:

$$\mathcal{K}_1(\tilde{\lambda}) = -\frac{i}{2} \left[I_1\left(\frac{n_1(\tilde{\lambda})}{\tilde{\lambda}}\right) + L_{-1}\left(\frac{n_1(\tilde{\lambda})}{\tilde{\lambda}}\right) - \frac{2}{\pi} \right] e^{-\frac{\pi}{\tilde{\lambda}}}, \quad (\text{B.26})$$

where we have introduced $n_1(\tilde{\lambda}) = N_1/m$. The factor $e^{-\frac{\pi}{\tilde{\lambda}}}$ makes $\tilde{\lambda} = \frac{2\sigma\hbar}{m^2} \rightarrow 0^+$ an essential singularity of $\mathcal{K}_1(\tilde{\lambda})$, and the prefactor is expandable in fractional powers of $\tilde{\lambda}$.

Denote the prefactor of (B.26) as:

$$\mathcal{I}(z) = \left(I_1(z) + L_{-1}(z) - \frac{2}{\pi} \right), \quad z = \frac{n_1(\tilde{\lambda})}{\tilde{\lambda}}, \quad (\text{B.27})$$

by using the continuation of semiclassical spectrum (see Sec.2), $n_1(\tilde{\lambda})$ can be expressed as:

$$n_1(\tilde{\lambda}) = 4 \left[\cosh \beta_1(\tilde{\lambda}) \cos \gamma_1(\tilde{\lambda}) - \cosh \vartheta_1(\tilde{\lambda}) \pm i \sinh \beta_1(\tilde{\lambda}) \sin \gamma_1(\tilde{\lambda}) \right], \quad (\text{B.28})$$

$$\text{with } \sinh 2\vartheta_1 - 2\vartheta_1 = \frac{3}{2}\pi\tilde{\lambda}, \quad \sinh 2\tilde{\vartheta}_1 - 2\tilde{\vartheta}_1 = -\frac{3}{2}\pi\tilde{\lambda}, \quad \tilde{\vartheta}_1 = \beta_1 \pm i\gamma_1. \quad (\text{B.29})$$

¹⁷Strictly speaking, with the negative coefficient of ρ^2 in (B.21), the path integration (B.22) is a counting of metastable states with negative modes, and is defined only via analytical continuation [26]. This fact introduces an extra factor of i in the coming (B.24). Also, the extra factor of $\frac{1}{2}$ in (B.24) is necessary, because there exist the negative mode $\rho = \text{Const}$, which corresponds to the variation of the bubble radius.

¹⁸To regulate $\int \mathcal{D}\rho e^{-\mathcal{S}}$, add $\delta\mathcal{S} = \frac{\epsilon}{\pi} \int_0^{2\pi} d\alpha \rho^2 = 2\epsilon(a_x^2 + a_y^2)$ to the action \mathcal{S} , with ϵ is the regulator. Denote ω as the "frequency" of the periodic boson, with $\delta\mathcal{S}$, the frequency shifts from $\omega^2 = -1$ to $\omega^2 = -1 + \frac{2\epsilon R}{\pi m}$. The path integration now becomes convergent, with:

$$\int \mathcal{D}\rho e^{-\mathcal{S} - \delta\mathcal{S}} = \frac{1}{2|\sinh \pi\omega|} \sim \frac{m}{2R} \frac{1}{\epsilon}.$$

On the other hand, gaussian integration yields $\int da_x da_y e^{-2\epsilon(a_x^2 + a_y^2)} = \frac{\pi}{2\epsilon} \rightarrow \text{Vol}(\mathbb{R}^2)$, and leads to (B.24).

Near $\tilde{\lambda} \rightarrow 0^+$, the function n_1 behaves as $n_1(\tilde{\lambda}) \sim \tilde{\lambda}^{2/3}$, thus $n_1/\tilde{\lambda}$ diverges with:

$$\frac{n_1(\tilde{\lambda})}{\tilde{\lambda}} = -\sqrt{3}e^{\mp\frac{\pi i}{6}}\left(\frac{9\pi}{8}\right)^{\frac{2}{3}}\tilde{\lambda}^{-\frac{1}{3}} + O(\tilde{\lambda}^{\frac{1}{3}}), \quad \text{with } a = \sqrt{3}\left(\frac{9\pi}{8}\right)^{\frac{2}{3}}. \quad (\text{B.30})$$

The expansion of $\mathcal{I}(z)$ at the large z is: (denote $\omega = e^{\frac{\pi i}{3}}$)

$$\mathcal{I}(z) \xrightarrow{\tilde{\lambda} \rightarrow 0^+} -\frac{2}{\pi} + \frac{\omega}{\pi a^2} \tilde{\lambda}^{\frac{2}{3}} \left[2 + 6\left(\frac{\omega \tilde{\lambda}^{\frac{2}{3}}}{a^2}\right) + 90\left(\frac{\omega \tilde{\lambda}^{\frac{2}{3}}}{a^2}\right)^2 + 3150\left(\frac{\omega \tilde{\lambda}^{\frac{2}{3}}}{a^2}\right)^3 \dots \right], \quad (\text{B.31})$$

where a was defined in (B.30). Based on the expansion (B.31), the leading contributions of $\mathcal{K}_1(\tilde{\lambda})$ reads:

$$\mathcal{K}_1(\tilde{\lambda}) = \frac{i}{\pi} e^{-\frac{\pi}{\tilde{\lambda}}} - \frac{16i}{27 \cdot 3^{\frac{2}{3}} \pi^{\frac{7}{3}}} \tilde{\lambda}^{\frac{2}{3}} e^{-\frac{\pi}{\tilde{\lambda}}} + O(\tilde{\lambda}^{\frac{4}{3}}), \quad (\text{B.32})$$

which is the instanton-like contribution to the mass of lightest particle in the metastable phase with $\xi \rightarrow 0^-$.

With similar strategies, one can compute the instanton-like contribution $\mathcal{K}_p(\tilde{\lambda})$ for any heavier excitation with mass M_p , by modifying the quantization condition (B.29) as $\frac{3}{2}\pi\tilde{\lambda} \rightarrow 2\pi\tilde{\lambda}(p - \frac{1}{4})$. The first term of $\mathcal{K}_p(\tilde{\lambda})$ expansion is $\frac{i}{\pi} e^{-\frac{\pi}{\tilde{\lambda}}}$, which is identical to the one of (B.32), because it comes from area of the cigar $\mathcal{C}(L, R_c)$. Subleading terms of $\mathcal{K}_p(\tilde{\lambda})$ have similar patterns comparing to (B.32), with different coefficients.

Finally, we back to the instanton-like contribution to the analysis of Sec.2 and Sec.3. Denote the universal leading contribution of $\mathcal{K}_p(\tilde{\lambda})$ as ($x = -\xi > 0$):

$$\mathcal{K}_0(\tilde{\lambda}) = \frac{i}{\pi} e^{-\frac{\pi}{\tilde{\lambda}}} = \frac{i}{\pi} e^{-\frac{\pi}{2sx}}, \quad (\text{B.33})$$

which should contribute to the discontinuities (2.4) at small negative ξ along the upper/lower edges of the Fisher-Langer's branch cut. The leading correction to $\Im m \hat{M}_p(\xi + i0)$ is:

$$\Im m \mathcal{K}_0(\tilde{\lambda}) = \frac{1}{\pi} e^{-\frac{\pi}{\tilde{\lambda}}} = \frac{1}{\pi} e^{-\frac{\pi}{2sx}}, \quad (\text{B.34})$$

which is as shown as the near horizontal magenta line in Fig.5. Obviously, comparing to the discontinuities from continuation ((2.5) and (2.9)), the contribution (B.34) is negligible.

On the complex η plane, the instanton-like contribution (B.32) should follow the continuation across the shadow domain. At the edges of low-T wedge $\text{Arg } \eta = \pm \frac{8}{15}\pi$, at large $|\eta|$ the \mathcal{K}_1 term contributes as:

$$\mathcal{M}_1(\eta) \rightarrow \mathcal{M}_1^{\text{exp}}(\eta = ze^{\pm\frac{8\pi i}{15}}) + \hat{\mathcal{K}}_1(z), \quad \hat{\mathcal{K}}_1(z) \rightarrow \frac{i}{\pi} e^{\pm\frac{8}{15}\pi} z e^{-\frac{\pi}{2s} z^{\frac{15}{8}}}, \quad (\text{B.35})$$

where $z = e^{\mp\frac{8\pi i}{15}}\eta$, and $\mathcal{M}_1^{\text{exp}}$ is the expansion of (3.15) with $\eta = ze^{\pm\frac{8\pi i}{15}}$. As illustrated in Fig.7, the continuation across the shadow domain is achieved by rotating η for $\frac{\pi}{5}$, as from the Fisher-Langer's branch cuts $\text{Arg } \eta = \pm \frac{8}{15}\pi$ to the rays of Yang-Lee branch cut $\text{Arg } \eta = \pm \frac{11}{15}\pi$.

Qualitatively, to obtain an exponential growth the exponent of (B.32) must have a positive real part. In other words, (B.32) changes its behaviours to oscillating growth after rotating ξ further for $\frac{\pi}{2}$ inside the Fisher-Langer's branch cut, or equivalently rotating η for $\frac{4}{15}\pi$ towards the shadow domain. With the angular size of shadow domain is $\Omega_{\text{SD}}^{(\eta)} = \frac{\pi}{5}$, the Stokes phenomenon of \mathcal{K}_1 term is hiding inside the Yang-Lee branch cut of Fig.7(b), and the M_1 extended analyticity is safe from extra singularities along the Yang-Lee branch cut.

Though by rotating $z \rightarrow ye^{\frac{\pi}{5}}$, (B.35) is exponentially small at $y \rightarrow +\infty$, quantitatively it's necessary to show that the contribution of (B.35) at finite y is sufficiently small, and the approximated $\Delta_1(y)$ from Appendix A remains intact. After rotating $z \rightarrow ye^{\frac{\pi}{5}}$, the contribution of $\Re \hat{\mathcal{K}}_1(y)$ and $\Im \hat{\mathcal{K}}_1(y)$ are as shown in Fig.8, with two solid lines which almost indistinguishable from the horizontal axis. As a result, the instanton-like terms of (B.35) are negligible on the interval $Y_0 < y < +\infty$, and can be ignored in the interpolation approach discuss in Appendix A.

Finally, despite that the instanton-like terms (B.32) and (B.35) only have tiny contribution to the low-T analyticity and extended analyticity of M_1 , they are implying something hiding within the Yang-Lee branch cut of Fig.7(b). The rotation of η for $\frac{4}{15}\pi$ towards the shadow domain would lead to the oscillating growth of $\hat{\mathcal{K}}_1$, and it suggests that the ray $\text{Arg } \eta = \pm\frac{4}{5}\pi$ may have interesting analyticity structures. One of the conjecture is that there exist an infinite number of singularities on the second sheet of η , within the Yang-Lee branch cut of Fig.7(b), and these singularities are condensing towards $|\eta| \rightarrow \infty$ along the ray $\text{Arg } \eta = \pm\frac{4}{5}\pi$. We will provide further detailed analysis in future works.

References

- [1] Hao-Lan Xu and Alexander Zamolodchikov. 2D Ising Field Theory in a magnetic field: the Yang-Lee singularity. *JHEP*, 08:057, 2022.
- [2] P Fonseca and A Zamolodchikov. Ising field theory in a magnetic field: analytic properties of the free energy. *Journal of statistical physics*, 110(3-6):527–590, 2003.
- [3] Alexander Zamolodchikov. Ising spectroscopy ii: particles and poles at $t > t_c$. *arXiv preprint arXiv:1310.4821*, 2013.
- [4] Hao-Lan Xu and Alexander Zamolodchikov. Ising Field Theory in a magnetic field: φ^3 coupling at $T > T_c$. 4 2023.
- [5] Vladimir V. Mangazeev, Bryte Hagan, and Vladimir V. Bazhanov. Corner Transfer Matrix Approach to the Yang-Lee Singularity in the 2D Ising Model in a magnetic field. 8 2023.
- [6] Chen-Ning Yang and Tsung-Dao Lee. Statistical theory of equations of state and phase transitions. i. theory of condensation. *Physical Review*, 87(3):404, 1952.
- [7] Tsung-Dao Lee and Chen-Ning Yang. Statistical theory of equations of state and phase transitions. ii. lattice gas and ising model. *Physical Review*, 87(3):410, 1952.
- [8] John L Cardy. Conformal invariance and the yang-lee edge singularity in two dimensions. *Physical review letters*, 54(13):1354, 1985.

- [9] Barry M McCoy and Tai Tsun Wu. *The two-dimensional Ising model*. Harvard University Press, 2013.
- [10] Michael E Fisher. Yang-lee edge singularity and ϕ^3 field theory. *Physical Review Letters*, 40(25):1610, 1978.
- [11] A.B. Zamolodchikov. Two point correlation function in scaling Lee-Yang model. *Nucl. Phys. B*, 348:619–641, 1991.
- [12] John L. Cardy and G. Mussardo. S Matrix of the Yang-Lee Edge Singularity in Two-Dimensions. *Phys. Lett.*, B225:275–278, 1989.
- [13] FA Smirnov and AB Zamolodchikov. On space of integrable quantum field theories. *Nuclear Physics B*, 915:363–383, 2017.
- [14] Alexei B. Zamolodchikov. Mass scale in the sine-Gordon model and its reductions. *Int. J. Mod. Phys. A*, 10:1125–1150, 1995.
- [15] A.B. Zamolodchikov. Integrals of Motion and S Matrix of the (Scaled) T=T(c) Ising Model with Magnetic Field. *Int. J. Mod. Phys. A*, 4:4235, 1989.
- [16] V. A. Fateev. The Exact relations between the coupling constants and the masses of particles for the integrable perturbed conformal field theories. *Phys. Lett. B*, 324:45–51, 1994.
- [17] G. Delfino, G. Mussardo, and P. Simonetti. Nonintegrable quantum field theories as perturbations of certain integrable models. *Nucl. Phys. B*, 473:469–508, 1996.
- [18] Vladimir Fateev, Sergei L. Lukyanov, Alexander B. Zamolodchikov, and Alexei B. Zamolodchikov. Expectation values of local fields in Bullough-Dodd model and integrable perturbed conformal field theories. *Nucl. Phys. B*, 516:652–674, 1998.
- [19] Oleg Alekseev. Form factors in the Bullough-Dodd related models: The Ising model in a magnetic field. *JETP Lett.*, 95:201–205, 2012.
- [20] Michael E Fisher. The theory of condensation and the critical point. *Physics Physique Fizika*, 3(5):255, 1967.
- [21] James S Langer. Theory of the condensation point. *Annals of Physics*, 281(1-2):941–990, 2000.
- [22] AF Andreev. Singularity of thermodynamic quantities at a first order phase transition point. *Sov. Phys. JETP*, 18:1415–1416, 1964.
- [23] NJ Gunther, DJ Wallace, and DA Nicole. Goldstone modes in vacuum decay and first-order phase transitions. *Journal of Physics A: Mathematical and General*, 13(5):1755, 1980.
- [24] MJ Lowe and DJ Wallace. Instantons and the ising model below t_c . *Journal of Physics A: Mathematical and General*, 13(10):L381, 1980.
- [25] CK Harris. The ising model below t_c : calculation of nonuniversal amplitudes using a primitive droplet model. *Journal of Physics A: Mathematical and General*, 17(3):L143, 1984.
- [26] M. B. Voloshin. DECAY OF FALSE VACUUM IN (1+1)-DIMENSIONS. *Yad. Fiz.*, 42:1017–1026, 1985.
- [27] Tai Tsun Wu, Barry M. McCoy, Craig A. Tracy, and Eytan Barouch. Spin spin correlation functions for the two-dimensional Ising model: Exact theory in the scaling region. *Phys. Rev. B*, 13:316–374, 1976.

- [28] Barry M McCoy and Tai Tsun Wu. Two-dimensional ising field theory in a magnetic field: Breakup of the cut in the two-point function. *Physical Review D*, 18(4):1259, 1978.
- [29] Gerard 't Hooft. A Two-Dimensional Model for Mesons. *Nucl. Phys. B*, 75:461–470, 1974.
- [30] Pedro Fonseca and Alexander Zamolodchikov. Ising spectroscopy. I. Mesons at $T < T(c)$. 12 2006.
- [31] S. B. Rutkevich. Formfactor perturbation expansions and confinement in the Ising field theory. *J. Phys. A*, 42:304025, 2009.
- [32] Pedro Fonseca and Alexander Zamolodchikov. Ising spectroscopy i: Mesons at $t < t_c$. *arXiv preprint hep-th/0612304*, 2006.